Recent Advances in Hybrid Sodium-Air Batteries

Xiaolong Xu [a,b,c], Kwan San Hui [c,*], Duc Anh Dinh [d] , Kwun Nam Hui [b, e*] and Hao Wang [a,*]

[a] The College of Materials Science and Engineering, Beijing University of Technology, Beijing, People's Republic of China

[b] Joint Key Laboratory of the Ministry of Education, Institute of Applied Physics and Materials Engineering, University of Macau, Avenida da Universidade, Taipa, Macau SAR, China.

[c] Engineering, Faculty of Science, University of East Anglia, Norwich, NR4 7TJ, United Kingdom

[d] NTT Hi-Tech Institute, Nguyen Tat Thanh University

[e] Department of Physics and Chemistry, Faculty of Science and Technology, University of Macau, Avenida da Universidade, Taipa, Macau SAR, China.

*Corresponding author:

E-mail: k.hui@uea.ac.uk (Kwan San Hui)

E-mail: bizhui@umac.mo (Kwun Nam Hui)

E-mail: haowang@bjut.edu.cn (Hao Wang)

Abstract: Among alkali-air batteries, aprotic sodium-air batteries (SABs) have attracted considerable attention owing to their high theoretical specific energy (1683 Wh kg^{-1}), high Na abundance, low-cost, and environment-friendliness. However, the application of SABs is currently restricted by their limited cycling life and low energy efficiencies due to insoluble and nonconductive discharge products (NaO_2 and Na_2O_2) generated on the air electrodes. By contrast, hybrid SABs (HSABs) have resolved these daunting challenges by adopting an aqueous electrolyte cathode via a unique solid ceramic-ion-conductor-layer design separating the aprotic and aqueous electrolytes, resulting in extended cycle life. Thus, HSABs have aroused immense attention as promising next-generation energy storage systems. However, HSABs still face the key challenge of unsatisfactory cycling life that hinders their practical applications. In this review, HSAB principles are introduced, the synthesis and rational designs of electrocatalysts based on the functions of oxygen reduction reaction/oxygen evolution reaction from other metal-air batteries are comprehensively reviewed for the purpose of providing insight into the development of efficient air electrodes for HSABs. Furthermore, research directions of the anode, electrolyte, and air electrodes toward high-performance HSABs are proposed.

Keywords: Hybrid Sodium-air Battery; Battery Principle; Electrocatalysts; Classification and Synthesis; Research Directions

1. Introduction

Recently, global energy crisis and environmental pollution from fossil fuels have aroused great concern from the public. Thus, alternative energy storage devices, and clean and renewable energy sources are vigorously sought [1, 2]. In this context, lithium (Li)-ion batteries (LIBs) have been extensively employed and applied in electric vehicles (EVs) [3, 4]. However, energy storages in extended range EVs require battery systems with substantially higher energy and power densities than current LIBs [5, 6]. Among various battery systems, including Li-sulfur batteries (LSBs) [7, 8, 9], Li-air batteries (LABs) [10-12], aluminum (Al)-air batteries (AABs) [13], and zinc (Zn)-air batteries (ZABs) [14, 15] (Table 1), sodium (Na)-air batteries (SABs) are the top candidates because of their high theoretical specific energy (1683 Wh kg^{-1}), high Na abundance, low-cost, and environment-friendliness [16, 17].

Table 1 Comparison of different batteries based on energy and resource.

Battery	Cathode	Anode	Energy density	References	Remarks
LIB	Lithium Compounds	Lithium/ Graphite	<500 Wh kg^{-1}	18	Distribution of lithium source is inhomogeneous and insufficient
LSB	Sulfur	Lithium	2600 Wh kg^{-1}	7	
LAB	Catalyzer	Lithium	5200 Wh kg^{-1}	10	
AAB	Catalyzer	Aluminum	500 Wh kg^{-1}	13	Low energy density
ZAB	Catalyzer	Zinc	700–850 Wh kg^{-1}	14	
SAB	Catalyzer	Sodium	>1600 Wh kg^{-1}	17	Suitable

A typical SAB consists of Na as the anode and a highly porous air electrode as the cathode; the anode and cathode are separated by a polymeric or ceramic separator and

are immersed in an electrolyte [19, 20]. Generally, SABs are classified according to the electrolytes used in the system. Two types of SABs: (1) aprotic and (2) hybrid aprotic/aqueous (referred to as "aqueous") SABs have been extensively studied [21, 22]. In an aprotic electrolyte, discharge products are usually insoluble and nonconductive metal oxides (NaO_2 and Na_2O_2), which are easily deposited on the pores of the air electrode; these products progressively cover active reaction sites and block O_2 diffusion pathways, thereby damaging batteries [23, 24]. To address the blocking of insoluble discharge products in the aprotic electrolyte, some researchers developed hybrid SABs (HSABs) by constructing Na/aprotic electrolyte/Na super ionic conductor (NASICON)/aqueous electrolyte/air electrode hybrid structures [23, 25, 26]. HSABs reduce discharge products clogging at the air electrode and the electrical conductivity deterioration of the air electrode due to insoluble discharge products, thereby enhancing cell discharge performance [27]. HSABs exhibit a higher standard voltage (3.11 V) and specific capacity (838 mAh g^{-1}) and lower overpotential than SABs [28]. Therefore, HSABs are promising next-generation high-energy density batteries.

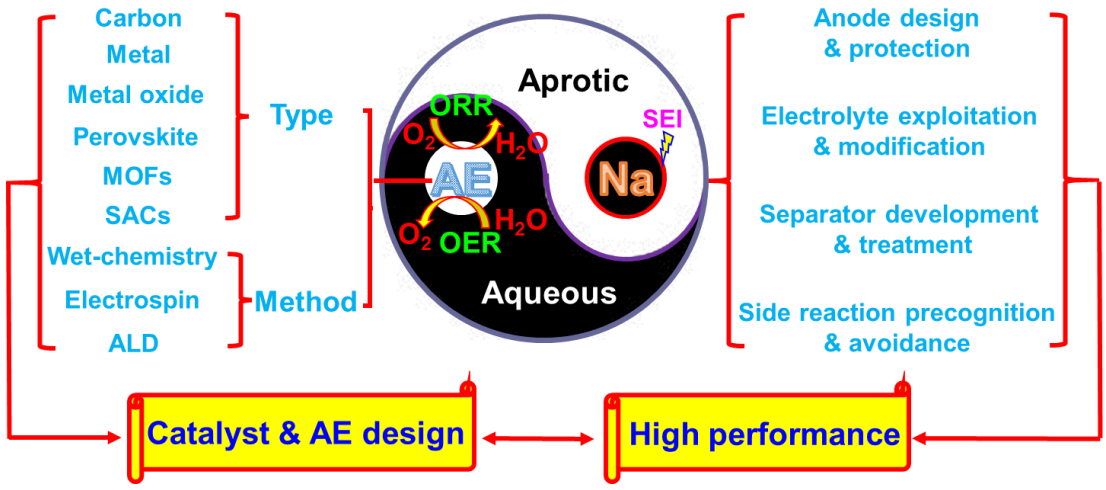

Fig. 1 Review scheme of opportunities, challenges, and potential research directions

for HSABs. AE is an air electrode.

Herein, we summarize the current progress of HSABs and the corresponding opportunities and challenges. The possible potential research directions for HSABs are outlined in Fig. 1. The design of catalysts for air electrodes involves catalyst type and synthesis method. The challenges and outlooks of HSABs are reviewed from various perspectives, including anode design and protection, electrolyte exploitation and modification, separator development and treatment, as well as side reaction precognition and avoidance based on their electrochemical reactions and components. We also comprehensively discuss electrocatalysts based on the reactions of oxygen reduction /oxygen evolution reactions from other metal-air batteries to provide a guide for designing desirable air electrodes and avoiding the potential side reactions (CO_2 poisoning and water evaporation) referenced from traditional fuel cells. Furthermore, several perspectives on potential research directions for the development of high-performance HSABs are proposed.

2. Principles of HSABs

2.1. Property of sodium

Na is an alkali metal with an atomic number of 11. Table 2 lists the properties and electrochemical performance of this element. The characteristics of Li are also presented in Table 2 for comparison with Na. In the Earth's crust, Li sources are limited and unevenly geometrically distributed [29]. Meanwhile, Na is the sixth most abundant

element and the fourth most abundant metal [30]. Compared with Li, Na is extremely inexpensive because it can be produced through the electrolysis of fused Na salts. In a battery system, Na is the second most electrochemically active metal after Li. Li and Na have reduction potentials (E_0) of −3.045 and −2.714 V, respectively. Therefore, Na is an outstanding alternative to Li [31]. The only drawback of Na is its high atomic weight (22.989 amu) compared to Li (6.941 amu). Thus, when used as the anode, Na decreases the theoretical specific capacity and energy density of a battery system. The theoretical specific capacity and energy density of Na are 1166 mAh g^{-1} and 3164 Wh kg^{-1}, respectively, and the energy density of Na batteries is higher than that of other battery systems (Table 1). Moreover, Na reacts with oxygen but not with nitrogen, whereas Li reacts with oxygen and nitrogen. Thus, Na is more suitable than Li for air batteries.

Table 2 Properties and electrochemical performance of Na and Li

Element	Na	Li
Atomic number	11	3
Atomic mass (amu)	22.989	6.94
Density (g cm^{-3})	0.968	0.534
Melting point (°C)	97.82	180.54
Boiling point (°C)	881.4	1317
Reserves	6th in the earth's crust	inhomogeneous and insufficient
Electronegativity (V)	−2.714	−3.045
Specific capacity (mAh g^{-1})	1166	3861
Energy density (Wh kg^{-1})	3164	11757
Dendrite formation	Yes	Yes
React with oxygen	Yes	Yes
React with nitrogen	No	Yes

2.2. Electrochemical reactions in HSAB

As metal-air batteries, HSABs employ dissolution/precipitation reactions rather than the intercalation mechanism during the electrochemical process [18]. The reactions occurring during charge-discharge at the cathode and the anode of HSAB can be described as follows [32]:

Cathode: $O_2 + 2H_2O + 4e^- \leftrightarrow 4OH^-$; $E_0 = +0.40$ V (1)

Anode: $Na \leftrightarrow Na^+ + e^-$; $E_0 = +2.71$ V (2)

Overall: $4Na + O_2 + 2H_2O \leftrightarrow 4NaOH$; $E_0 = 3.11$ V (3)

Based on the above equations, the standard cell voltage is 3.11 V. Moreover, when the pH of the aqueous electrolyte (0.1 M NaOH) is considered, the theoretical voltage of the HSABs is ~3.17 V [19].

In contrast, the reactions in aprotic SABs are described as follows [33]:

Cathode: $O_2 + e^- \leftrightarrow O_2^-$; $E_0 = -0.44$ V (4)

or $O_2 + 2e^- \leftrightarrow O_2^{2-}$; $E_0 = -0.38$ V (5)

Anode: $Na \leftrightarrow Na^+ + e^-$; $E_0 = +2.71$ V (6)

Overall: $Na + O_2 \leftrightarrow NaO_2$; $E_0 = 2.27$ V (7)

or $2Na + O_2 \leftrightarrow Na_2O_2$; $E_0 = 2.33$ V (8)

Notably, the charge-discharge reactions of HSABs involve a simple reaction process and single discharge product (NaOH) compared with those (NaO_2 or Na_2O_2) in SABs. The simple reaction process significantly reduces the occurrence of side reactions, thereby increasing the cycle life of a battery. Furthermore, the single

discharge product NaOH is soluble in the aqueous NaOH electrolyte, which avoids the accumulation of discharge products on the surface of the air electrode, and thus enhances the efficiency of the battery. In addition, HSABs offer a higher theoretical voltage (3.11 V) than that of SAB (2.33 V), which is the key parameter for the high energy density of a battery system.

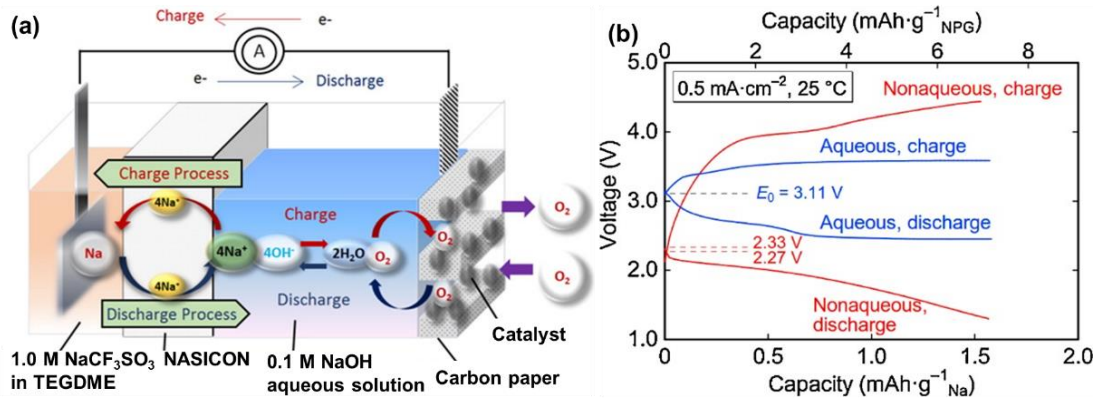

Fig. 2 (a) Schematic and charge–discharge process of HSABs [19]. Copyright 2015, Elsevier. (b) First discharge–charge curves of aqueous (HSAB) and nonaqueous (SAB) at 0.5 mA·cm^{-2} [34]. Copyright 2015, Elsevier.

In contrast to the intercalation reaction, the dissolution/precipitation reaction involves the evolution of the crystal structure of electrode material. Fig. 2a shows a schematic and charge-discharge processes of HSABs [19]. In the discharge process, Na is oxidized into Na ions, which diffuses from the anode to the cathode through a NASICON separator. At the same time, electron transport via external circuit from the anode to the cathode, where oxygen reduction reaction (ORR) occurs. During the charging process, Na ions from the cathode diffuse into the anode through the

NASICON separator; the oxygen evolution reaction (OER) occurs at the cathode, and Na ions deposit as neutral Na on the Na anode. Fig. 2b shows the charge-discharge curves of SAB and HSAB [34], which are based on the above electrochemical reaction mechanism (Equations 1-8).

In contrast, during the discharge process of an aprotic SAB, Na ions from the anode move through the electrolyte toward the cathode. Oxygen molecules are reduced before combining with the Na ions to form discharge products, namely sodium oxide, on the surface of the air electrode. The insoluble discharge products severely impede the electroactive surface area of the air electrode and kinetics of the ORR [35, 36], resulting in the short cycle life of SABs. To resolve the insoluble discharge products, HSABs, composed of a NASICON separating the aprotic and aqueous electrolytes were developed. As a result, the cycle life of HSABs is significantly extended.

In metal-air batteries, the OER is a critical reaction that generates molecular oxygen through several proton/electron coupled processes [37, 38]. In alkaline conditions, the oxidation of hydroxyl groups (OH^-) predominates, which are transformed into H_2O and O_2, and involves the same number of electrons [39]. As OER is an electron-coupled uphill reaction, which corresponds to the oxygen evolution during the charge of HSABs, as shown in Eq (9) [40]:

$$4OH^- \leftrightarrow 2H_2O + O_2 + 4e^- \quad (9)$$

$$E = E^0 - \frac{RT}{nF} \ln \frac{[Red]}{[Ox]} \quad (10)$$

where E is the cell potential, $E°$ is the cell potential at standard conditions, R is the ideal gas constant, T is the temperature in Kelvin, n is the number of moles of electrons

involved for each mole of reaction, *F* is the Faraday constant, [Red] is the concentration of reduced molecules, and [Ox] is the concentration of oxidized molecules. According to the Nernst Eq (10), the potential is dependent on pH by shifting 59 mV for each pH unit increase. Thus, the oxygen production voltage of HSABs can be controlled by adjusting the pH of the aqueous electrolyte. The generation of each O_2 molecule requires a transfer of four electrons. OER usually involves multiple steps; each step in turn involves a single electron transfer process because multi-electrons transfers at one time are not kinetically favorable [41, 42]. Cheng et al. [43] presented the detailed mechanism of OER reaction taking lattice-strained metal-organic framework (MOF) array as an example (Fig. 3a). The first deprotonation of the surface-adsorbed OH on Ni sites converts the surface Ni^{3+}–OH group into Ni^{3+}–O· (step I). Then, the generation of superoxide *OOH species on the Ni^{4+} sites (superoxide Ni^{4+}–OOH, step II) leads to further deprotonation of superoxide OOH species (step III) and the release of an O_2 molecule to recover the initial state of Ni^{3+}–OH (step IV). In HSABs, ORR is a process of oxygen adsorption and catalytical reaction. A full reduction is a dissociative adsorption process, which begins with O_2 adsorption on a catalyst surface [44, 45]. The detailed ORR mechanism (Fig. 3b) reported by Cheng et al. [43] is described below. The fast O_2/OH˙ exchange realizes to produce O_2˙ radical species on Ni sites (step I). Consequently, this O_2˙ radical is further protonated by a H_2O molecule to yield superoxide *OOH, accompanied by the oxidation of Ni^{3+} into Ni^{4+} to form a Ni^{4+}–OOH intermediate (step II). After that, further protonation of the distal O in Ni^{4+}–OOH (step III) and the fourth proton-coupling electron transfer (step IV) leads to the cleavage of

O–O and then the recovery of the Ni sites to the original state of Ni^{3+}–OH. It is the fast and efficient $4e^-$ OER processes for the lattice-strained MOFs.

The electrocatalyst involved in the OER and ORR needs good electrical conductivity to promote electron transport. Therefore, the development of desirable electrocatalysts is expected to expedite reaction kinetics and to lower the overpotential. Few non-precious metal oxides can survive under oxidative potentials in acidic conditions [46]; thus, researchers have been searching for non-precious metal-based candidates for electrocatalysts in alkaline conditions, in which most metal oxides or hydroxides are chemically stable. An ideal electrocatalyst for HSABs should have high conductivity, low overpotential, high durability, low-cost, high earth abundance, and high scalability.

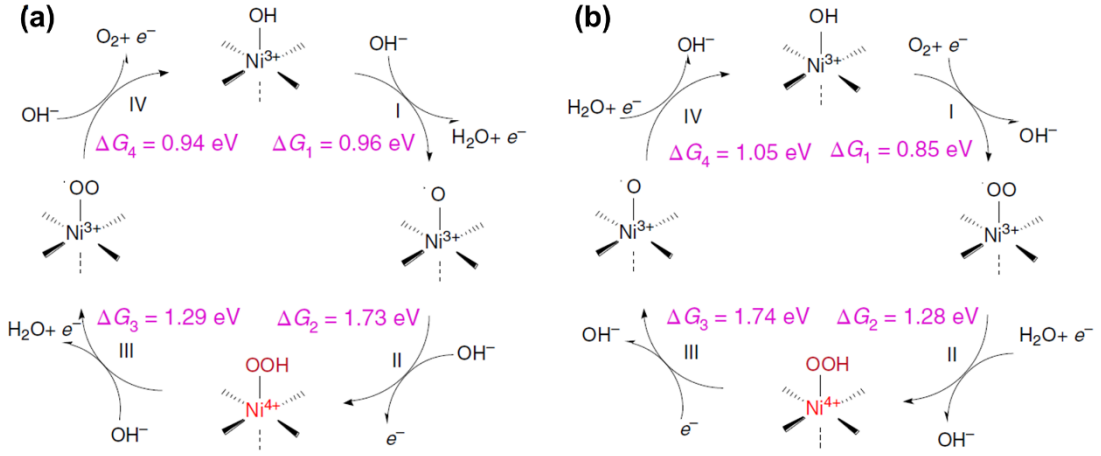

Fig. 3 Proposed OER (a) and ORR (b) catalytic mechanisms for the lattice-strained metal-organic frameworks (MOFs) [43]. Copyright 2019, Springer.

2.3. Components of HSABs

Na anode, air electrode, electrolyte, and NASICON separator are the main components of the HSABs [47-51]. Table 3 summarizes the details and performance of the reported HSABs in literature. Typically, air electrodes are composed of a gas permeable layer, a catalytic layer, and a current collector [52]. Unlike SAB, HSAB requires aqueous electrolyte on its air electrode side, while aprotic electrolyte on its anode side [27]. A simple HSAB structure was first designed by Liang et al. [53]. A Na foil was applied as the anode, graphene sheets were used as catalysts in the catalyst layer. An aqueous electrolyte of 1 M NaOH and the aprotic electrolyte of 1 M $NaClO_4$ in EC/DMC (1:1) were used with the insertion of NASICON (1 mm in thickness, 10 mm in diameter) as the separator.

Table 3 Cathode, aqueous electrolyte, separator, aprotic electrolyte and electrochemical performance of HSABs.

	Cathode	Aqueous electrolyte	Separator	Aprotic electrolyte	Overpotential (V)	Power density	Round trip efficiency (%)	Stability	Ref.
Carbon-based	Graphitic nanoshells @ mesoporous carbon	0.1 M KOH	$Na_3Zr_2Si_2PO_{12}$, 8.9×10^{-4} S cm^{-1}	1 M $NaCF_3SO_3$ in tetraethylene glycol dimethyl ether	0.72	78.2 mW g^{-1} at 60 mA g^{-1}	96.28	Excellent charge–discharge stability	52
	Graphene sheets	1 M NaOH	NASICON, 1.3×10^{-3} S cm^{-1}	1 M $NaClO_4$ in EC/DMC (1:1)	-	13.8 mW cm^{-2} at 1 mA cm^{-2}	-	-	53
	Carbon felts	0.1 M CA and 1 M $NaNO_3$	$Na_{1+x}Zr_2SixP_{3-x}O_{12}$, x = 2, 10^{-3} S cm^{-1}	1 M $NaCF_3SO_3$ in tetraethylene glycol dimethyl ether	~0.4	-	-	Over 20 cycles at 0.1 mA cm^{-2}	54
Metal-based	Nanoporous gold	1 M NaOH	NASICON ceramics，1.4×10^{-3} S·cm^{-1}	1 M $NaClO_4$ and 1 vol% fluoroethylene carbonate in EC/DMC	~0.6	12.4 mW·cm^{-2}	80	Up to 18 cycles	34
	Pt/C powder	0.1 M H_3PO_4 + 0.1 M Na_2SO_4 + 0.1M HAc+0.1MnaAc	$Na_3Zr_2Si_2PO_{12}$, 1.3×10^{-3} S cm^{-1}	1 M $NaClO_4$ in ethylene carbonate/dimethyl carbonate with 1 vol% fluoroethylene carbonate	0.3	34.9 mW cm^{-2}	90	30 cycles	55

Metal oxide-based	Porous cobalt manganese oxide	0.1 M NaOH	$Na_{1+x}Zr_2SixP_{3-x}O_{12}$, x = 2, 10^{-3} S cm^{-1}	1 M $NaCF_3SO_3$ in tetraethylene glycol dimethyl ether	0.53	-	79	100 cycles	56
	$MnCo_2O_4$ @ N-doped reduced graphene oxide	1 M NaOH	$Na_3Zr_2Si_2PO_{12}$, 1.3×10^{-3} S cm^{-1}	1 M $NaClO_4$ in EC/DMC (1:1) with 1 vol% FEC	0.39	-	87.6	No significant degradation during the 25 cycles	47
	VO_2 on rGO-coated carbon paper	0.1 M NaOH	$Na_3Zr_2Si_2PO_{12}$, 8.9×10^{-4} S cm^{-1}	1 M $NaCF_3SO_3$ in tetra ethylene glycol dimethyl ether	0.64	104 mW g^{-1} at 80 mA g^{-1}	81	Up to 50 cycles.	11
	Mn_3O_4/C	0.2 M NaOH	$Na_3Zr_2Si_2PO_{12}$, 1.3×10^{-3} S cm^{-1}	0.2 mL Na[FSA–C2C1im][FSA]	-	27.6 mW cm^{-2} at 50 °C	-	Specific capacity of 835 mAh g^{-1} at 50 °C	47
	$Tl_2Rh_2O_7$	1 M NaOH	NASICON	1 M $NaCF_3SO_3$/TEGDME	0.208	159.9 mW g^{-1} at 120 mA g^{-1}	93.65	excellent cycling stability up to 50 cycles	49
	$Bi_2Ru_2O_7$ nanoparticles	1 M NaOH	NASICON	1 M $NaCF_3SO_3$/TEGDME	0.211	156.32 mWg^{-1} at 120 mA g^{-1}	93.58	excellent cycling stability up to 50 cycles	50
MOFs-based	Metal-organic framework (MOF)-derived N-doped carbon Nanotubes	1M NaOH	$Na_3Zr_2Si_2PO_{12}$, 1.3×10^{-3} S·cm^{-1}	1M $NaClO_4$ in EC/DMC(1:1) with 1-vol % FEC	0.3	-	87	charge voltage increases from 3.12 to 3.30 V at 0.1 mA·cm^{-2} for 35 cycles	51
Others	3D SnS_2 nanopetals	0.1 M NaOH	NASICON ceramic plate	1 M $NaCF_3SO_3$ in tetraethylene glycol dimethyl ether	0.52	300 mW g^{-1} at 240 mA g^{-1}	83	Recharge ability of 40 cycles at 5 mA g^{-1}	57

1

2.3.1. Air electrode

In the cell components, the air electrode is the reaction site for adsorption, oxygen reduction, and oxygen evolution reactions during the charge-discharge cycle [21, 58]. The air electrodes of the aprotic SABs, serving as media to accommodate solid discharge products such as Na_2O_2 or Na_2O [55, 54]. To facilitate the ORR/OER in metal-air batteries, the ideal air electrode should have adequate porosity and suitable pore volume and pore size distribution in addition to general electrode characteristics, such as electronic conductivity, chemical stability, high surface area, and low-cost [59, 60]. Furthermore, the final performance of metal-air batteries strongly depends on air electrode efficiency [56].

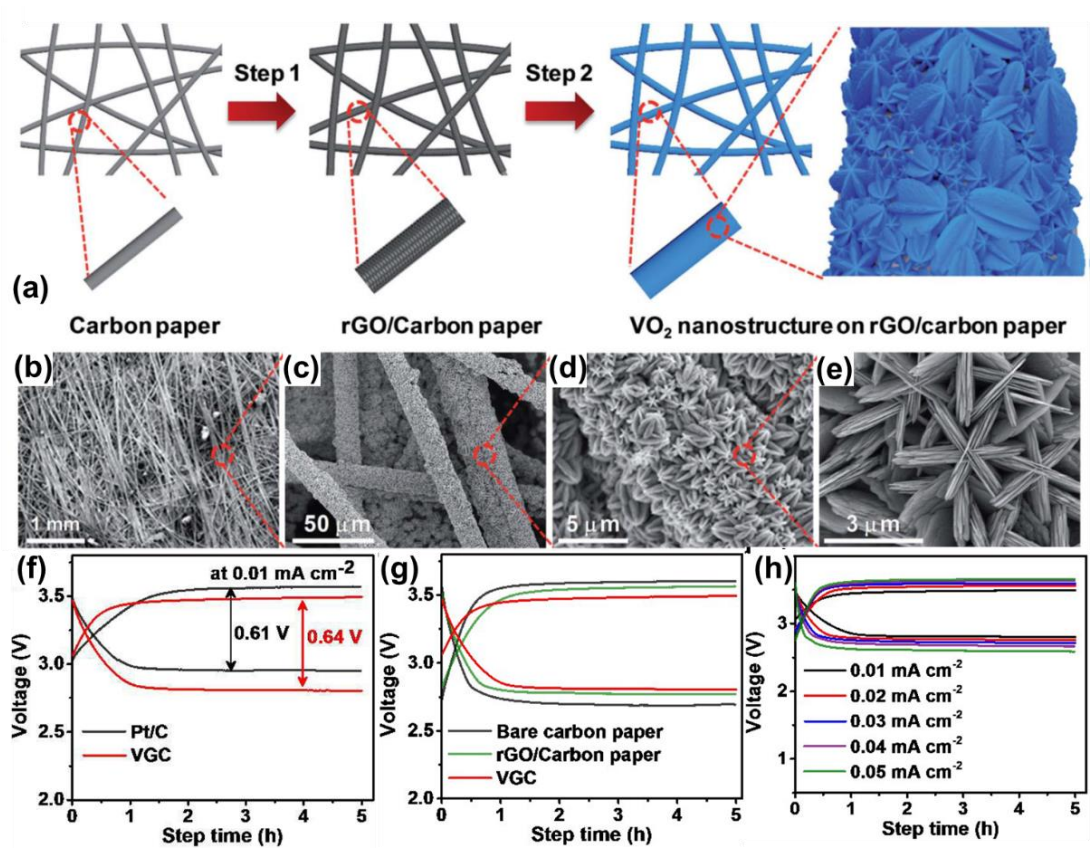

Fig. 4 (a) Schematic for air electrode fabrication. (b, c) Low-magnification and (d, e)

high-magnification scanning electron microscope (SEM) images of the prepared binder-free air electrode. The SEM images show the formation of carambola-shaped VO_2 nanostructures on the reduced graphene oxide (rGO)-coated carbon paper. (f) Charge-discharge profile of the assembled Na-air cell using VO_2 nanostructures on rGO-coated carbon paper (VGC) and Pt/C air electrodes at a current density of 0.01 mA cm^2. (g) Comparative charge-discharge profile of the assembled Na–air cell using bare carbon paper, rGO/carbon paper, and VGC air electrode. (h) Rate capability test of VGC electrode at different scan rates [11]. Copyright 2014, Elsevier.

Generally, the air electrodes of metal-air batteries are composed of three main components: (1) catalytic layer (catalysts and conductive agents bonded together by a binder), (2) current collector (metal foam, stainless steel mesh, carbon paper, etc.), and (3) gas permeable layer (breathable and H_2O-impermeable polymer). Recently, binder-free air electrodes for metal-air batteries, preventing “dead volume” due to the addition of conductive agents and polymer binders, have attracted considerable attention because of their reduced path lengths for ion transport; these features allow an enormous increase in the number of catalytic sites for ORR/OER. Khan et al. [11] synthesized vanadium oxide (VO_2) nanostructures on reduced graphene oxide (rGO)-coated carbon paper by a hydrothermal growth for rechargeable HSABs; the nanostructures showed a carambola morphology and served as a novel binder-free and bifunctional electrocatalyst (Fig. 4a). SEM images showed the uniform growth of the VO_2 nanostructures on the rGO-coated carbon paper (Figs. 4b and 4c), and the sample

was composed of uniform microsized ellipsoidal structures with a carambola morphology (Figs. 4d and 4e). Because of no binder, the specific surface area of the catalyst is larger and more active sites are exposed to the surface. It is conducive to the improvement of catalytic activity. The prepared sample displayed a specific surface area of 6.3 m^2 g^{-1}. As the air electrode of an HSAB, the fabricated cell displayed a comparable overpotential gap of 0.64 V (Fig. 4f) compared to that of Pt/C catalysts (0.61 V), and an improved charge-discharge curves and rate capabilities at different current densities ranging from 0.01 mA cm^{-2} to 0.05 mA cm^{-2} (Figs. 4g and 4h). Liu et al. [61] designed a $NiCo_2O_4$ nanosheet supported on a Ni foam through a solvothermal method. As a carbon-free and binder-free air electrode, $NiCo_2O_4$ nanosheet/Ni exhibited an initial discharge capacity of 1762 mAh g^{-1} and a low overpotential of 0.96 V at 20 mA g^{-1}, indicating its potential for rechargeable HSABs. These studies concluded that binder-free air electrodes play an important role in reducing the overpotential of HSABs, thereby resulting in enhanced electrocatalytic performance. The studies provided a satisfactory guide for the development of promising electrodes for high-performance HSABs. Exposure of more catalytic sites is the key to improve the catalytic performance of air electrodes, which is also an important reference for the rational design of catalysts and air electrodes.

2.3.2. Anode

Active anode materials of HSABs are Na, modified Na, and Na alloy [62]. In our previous studies, we reviewed the issue of Li dendrite growth in Li batteries [18, 63].

Li dendrite exhibited a preferential orientation growth face on the Li surface under nonequilibrium conditions, such as high current density and low working temperature [64]. We mainly attributed this orientation to the intrinsic feature of Li-ion electromigration during nucleation and growth processes [65]. Although Li as an anode material has an extremely high energy density, dendrite growth during charge-discharge processes severely limits its capabilities [66]. Na dendrite growth is more extensive during the charge-discharge cycles of HSABs compared with Li dendrites growth because Na intrinsically presents more active chemical properties and easier orientation growth than Li [67, 68]. In HSABs, dendritic growth may form along the edge and microstructures of the NASICON separator and can cause performance degradation and serious safety issues. Dendrites reach the air electrode can cause a short circuit, resulting in smoke or even fire, especially in the presence of volatile organic electrolytes. Moreover, an aqueous electrolyte can reach an anode and react with Na, resulting in explosion and fire [69, 70], and cell destruction may occur when aqueous and organic electrolytes combine. Therefore, Na dendrite is a major challenge to the development of HSABs and the Na anode protection is a focus of HSAB research. Dendrite growth can be suppressed by facilitating the formation of stable solid electrolyte interphase (SEI) layer on the Na anode through the surface treatment of the anode and the electrolyte modification by utilizing various organic solvents, sodium salts, and/or functional additives [71].

In the initial stage of the electrochemical reaction, the non-uniform charge distribution on the Na anode surface caused by the side reaction easily leads to dendrite

growth. Zhao et al. [25] reported that the reaction between sodium and liquid electrolytes forms an unstable SEI on the surface of the Na anode, leading to mossy or dendritic Na growth due to nonuniform ionic flux during repetitive Na stripping/plating (Fig. 5a). Dendrites and mossy Na formation can be suppressed by protecting the Na anode with a controllable inorganic-organic coating with the use of an advanced molecular layer deposition method (Fig. 5b). The key to prevent dendrite growth is to form a good SEI film on the surface of Na anode in the early stage of the electrochemical reaction. Wu et al. [72] reported an accessible method to grow a durable protective passivation film on Na anode surfaces. No dendrite formed during long-term stripping/plating cycles because of the sodium fluoride-rich film (Figs. 5c and 5d). Moreover, the design of the electrode structure is also a strategy to inhibit dendrite growth, and can effectively improve the electrochemical performance of HSABs. In 2018, Liang et al. [22] presented a new high-performance rechargeable HSAB with an organic liquid anode, which was prepared by dissolving Na into a solution of biphenyl and ether; the anode acts not only as the liquid anode but also as the organic electrolyte. The liquid anode-based HSAB demonstrated satisfactory reversibility and improved power density. Their study provided an important guide for the development of safe and high-performance HSAB anodes. These efforts and developments resulted in the production of safe HSABs with impressive discharge-charge capability. For future research of Na anode, the dendrite growth on the surface of the Na anode may be inhibited by interfacial modification (e.g. coating and enhancing surface area), Moreover, other structural design of anode, such as porous

anode and powder anode may be the new routes for Na protection and high-performance HSABs.

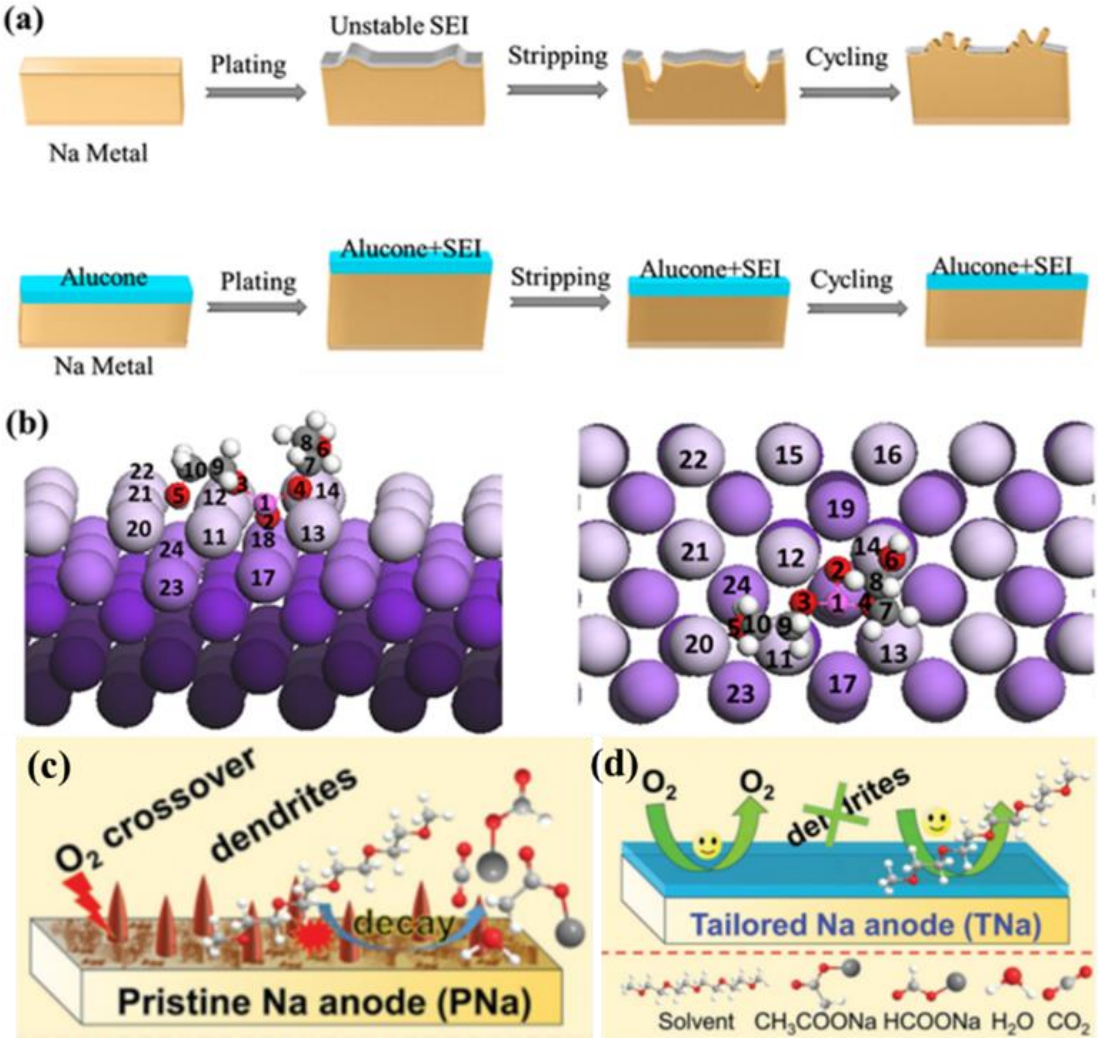

Fig. 5 (a) Schematic of Na stripping/plating on bare Na foil and Na foil with molecular layer deposited-alucone coating. (b) 3 dimension (D) and top views of adsorption of a single alcuone molecule on the Na (100) surface (four possible different binding sites: top, short-bridge, long-bridge, and 4-fold hollow) [25]. Copyright 2017, American Chemical Society. (c) Illustration of O_2 crossover, dendrite formation, and electrolyte decay on the pristine Na anode in a Na–O_2 battery. (d) Illustration of improvements on TNa [72]. Copyright 2018, Wiley.

2.3.3. Electrolyte

The electrolytes are the highly distinctive components of HSABs. HSAB electrolytes consist of two parts: aprotic and aqueous electrolytes. These parts are separated by a NASICON separator [20]. The commonly used aqueous electrolyte solution in the air electrode is NaOH solution with a concentration range of 0.1–1.0 M [11]. Typically, aqueous KOH, $NaNO_3$, and acidic Na salt solutions are used for HSABs [54]. The remarkable advantage of the aqueous electrolyte is its ability to prevent the deactivation of the air electrode catalyst caused by the deposition of discharge products. Na salts, such as $NaCF_3SO_3$, $NaClO_4$, and Na[FSA–C2C1im][FSA], are dissolved in organic solvents, such as tetra (ethylene glycol) dimethyl ether (TEGDME) and ethylene carbonate/dimethyl carbonate (EC/DMC), to form the anode electrolyte [73]. To improve the stability of electrolytes, fluoroethylene carbonate (FEC) is applied as an additive in the organic electrolyte [74]. The stability of the organic electrolyte in HSABs is a challenge that needs to be solved.

An ideal electrolyte should tolerate a highly oxidative environment for long cycling requirement and reversible participation in electrochemical reactions. The electrolyte is related to the formation of SEI film on the Na surface during the initial stage of the charge-discharge cycle. A perfect SEI film can effectively prevent side reactions between the organic electrolyte and electrodes, thereby improving the stability of cells. Unstable SEI films may lead to the formation of Na dendrites and may thus diminish performance and safety [75]. In summary, Na salt, organic solvents, and electrolyte additives may influence the formation of SEI films.

Lutz et al. [76] investigated the influence of different Na salt anions (PF_6^-, ClO_4^-, OTf^-, and $TFSi^-$) on the performance of SABs (Fig. 6). The stability of the SEI films highly depended on the kind of sodium salt used. The long-term stability of the films was determined by measuring the cycling tests. The electrolytes using NaTFSi are absolutely detrimental to metallic sodium, and employing NaOTF and $NaClO_4$ leads to short-term stability. Moreover, only the combination of 1,2-dimethoxyethane $NaPF_6$ greatly improved the efficiency and performance of the SEI films. In other words, when $NaPF_6$, NaCl, and NaOTF were used, the sodium metal was covered by a gray or bluish SEI.

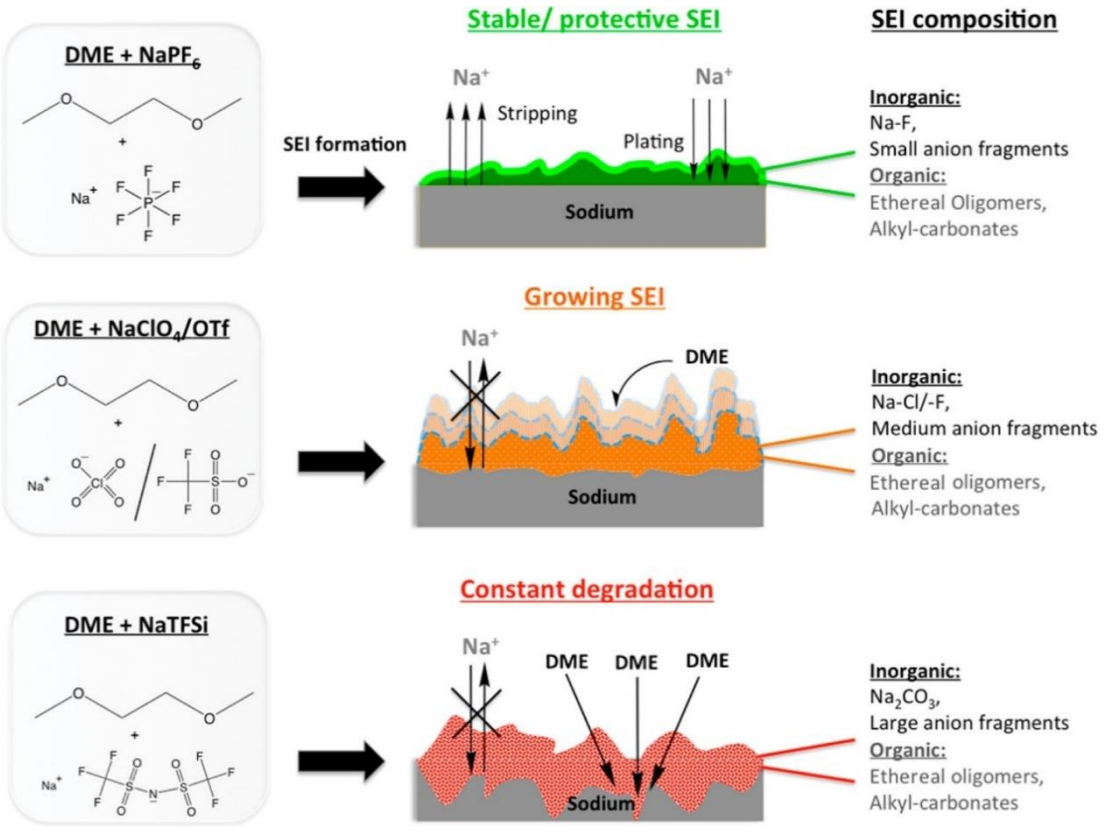

Fig. 6 Illustration of the proposed mechanism of Na SEI formation and its composition in different dimethoxyethane (DME) electrolytes [76]. Copyright 2017, American Chemical Society.

Organic solvents and additives play an important role in the regulation of SEI film formation on a Li surface. Such insight is a valuable guide for the study of HSAB electrolytes. For example, organic electrolytes, such as 1-ethyl-3-methylimidazolium bis(trifluoromethanesulfonyl)imide [77], lithium bis(trifluoromethane sulfonyl)imide (LiTFSI) [78], and N-methyl-N-allylpyrrolidinium bis(trifluoromethanesulfonyl)imide (RTIL P_1A_3TFSI) [79], have been demonstrated to effectively tune SEI films on Li surfaces owing to their desirable physical and chemical properties, such as nonflammability, negligible vapor pressure, high Li ion conductivity, and wide electrochemical window. Ma et al. [80] reported that N-methyl-(N-butyl) pyrrolidinium bis(trifluoromethanesulfonyl) imide (PYR_{14}TFSI) could suppress the growth of Li dendrites by regulating the formation of stable and uniform SEI films. Kim et al. [81] pioneered the use of $CsNO_3$ as an electrolyte additive for the formation of stable SEI layers on Li surfaces in LSBs. Therefore, studies toward finding a stable organic solution and effective additive for HSABs is an ongoing research subject. The electrolyte modification references from LIBs and traditional SABs can be useful guidelines for the development of high-performance HSABs.

2.3.4. Separator

The separators of all energy storage devices are inactive fundamental components, which are sandwiched between the anode and cathode [82]. Generally, the separator has two important functions: (1) providing a path for ionic conduction throughout the interconnected porous structure and (2) separating the anode and cathode to prevent

internal short circuit. The separators for liquid electrolyte batteries are engineered as porous membranes, nonwoven mats, or multilayers consisting of porous membranes and/or nonwoven mats [83, 84]. In HSABs, separators play other important roles: (1) preventing the mixing of solvents in the two electrolytes, (2) ensuring the passage of Na ions from the Na anode to the air electrode, and (3) reducing safety problems caused by the reaction between aqueous electrolyte and Na [85].

NASICON is a well-known sodium-ion-conducting oxide ceramic that has the general formula: $Na_{1+x}Zr_2Si_xP_{3-x}O_{12}$ ($0<x<3$) [86]. Diverse compositions were studied and ceramics with high conductivities were obtained when x was close to 2. The conductivities of NASICON ceramics are higher than 10^{-3} S cm^{-1} at room temperature [87, 88]. Moreover, manufacturing NASICON ceramics is economical because they are synthesized in air from abundant elemental sources [89].

Noi et al. [89] studied the liquid-phase sintering of NASICON, using a Na_3BO_3 (NBO) additive to lower the NASICON sintering temperature. A dense NASICON-based ceramic was obtained by sintering at 900 °C with 4.8 wt.% NBO. This liquid-phase sintered NASICON ceramic exhibited a high conductivity of ~1×10^{-3} S cm^{-1} at room temperature and low conduction activation energy of 28 kJ mol^{-1}. The conductivities at room temperature were 1.4×10^{-3} S cm^{-1} and 1.1×10^{-3} S cm^{-1} in ceramics sintered at a low temperature (900 °C) and high temperature (1220 °C), respectively (Figs. 7a–7c). Liang et al. [90] prepared a dense $Na_3Zr_2Si_2PO_{12}$ ceramic at low temperatures with an ionic conductivity of 1.3×10^{-3} S cm^{-1} at 25 °C as a separator for HSABs (Figs. 7d–7e). No substantial structural change was found between the

ceramic separator of the as-prepared state and the ceramic separator immersed in 1 M NaOH electrolyte for 2 days, thereby indicating acceptable stability of the prepared ceramic separator (Figs. 7f–7h). The HSAB yielded a maximum output power density of 21 mW cm^{-2} at 25 °C because of the reduced ohmic resistivity of the ceramic separator. Since then, the development of HSABs was significantly promoted. However, The mechanism of Na ion transport in NASICON is not clear, which will hinder the further modification of NASICON and the development and application of new separators. With the development of flexible electronic devices, flexible energy storage battery became a new research focus [91, 92]. Although the development of flexible separators is a huge challenge, the development of flexible metal-air batteries is expected to attract considerable attention from the academe and industries owing to the increasing demand for portable electronic devices. Therefore, the development and modification of new separators are also the next research focus on high-performance HSABs.

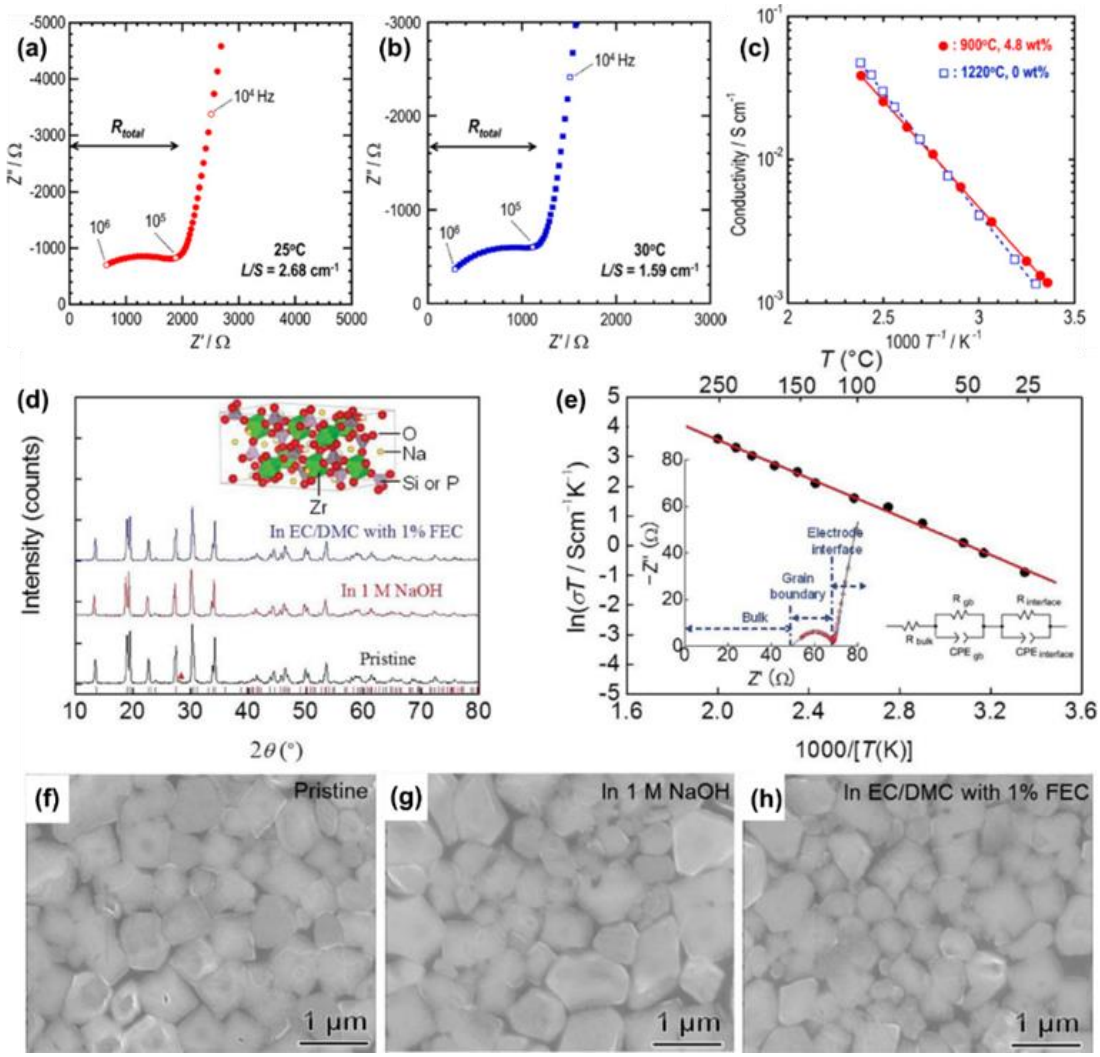

Fig. 7 Nyquist plots at room temperature (a, b) and temperature dependence of total conductivities (c) of NASICON ceramics with large L/S value. (a) Ceramic sintered at 900 °C with 4.8 wt.% NBO. (b) Ceramic sintered at 1220 °C without NBO [89]. Copyright 2018, American Chemical Society. (d) XRD patterns of the pristine NASICON ceramic separator before and after discharges. The triangle indicates the zirconia precipitate. Inset shows a crystal model of NASICON. (e) Arrhenius plot of the conductivities of the NASICON ceramic separator. Inset is a Nyquist plot of the impedance spectrum at 25 °C and an equivalent circuit model for the fitting. SEM images of NASICON ceramic separators at (f) as-prepared state, (g) after immersion in

1 M NaOH for two days and (h) after immersion in 1 M $NaClO_4$ in EC/DMC with 1% FEC for two days [90]. Copyright 2015, ECS.

2.4. Potential influencing factors for HSABs stability

In addition to the existing challenges from the components of metal-air batteries, several problems such as CO_2 poisoning [93] and water evaporation [94, 95] that influence the catalytic activity of air electrodes and the performance of batteries have drawn considerable attention from academe and industries and need to be solved.

2.4.1. CO_2 poisoning

CO_2 poisoning is regarded as the main catalyst deactivation process after the reaction between catalyst and CO_2. This catalyst deactivation process generally leads to consequence inactive of catalyst and short cycle life of devices. Divekar, et al. showed that a low concentration of CO_2 (300-400 ppm) in atmospheric air has significantly influenced on the chemistry of anion exchange membrane fuel cell and ultimately led to decrease in fuel cell performance [96]. Their study concluded that the drop of OH^- ion concentration within minutes because of the formation of HCO_3^- and CO_3^{2-} with OH^-. The degrade of fuel cell performance was attributed to the decrease of anionic conductivity because HCO_3^- and CO_3^{2-} have lower mobility than OH^-. A similar study showed that CO_2 is highly soluble in aprotic and aqueous electrolytes and highly reactive toward Li, Na, and their oxides and hydroxides to form carbonates [97]. Especially, the formation of carbonates through parasitic reactions in Li- and Na-air

cells is unfavorable for metal-air batteries due to the high decomposition potential of carbonate-based products [98]. Several studies have shown that carbonates were formed as a result of the reactions involving the oxidation of solvents [99] and carbon cathodes [100] as well as chemical reactions between LiO_x/NaO_x and CO_2. Mekonnen et al. [101] proved that once CO_2 is adsorbed on a step valley site of Li_2O_2 discharge product in Li-air battery, it is hardly diffuse and affect the Li_2O_2 growth mechanism, device's capacity and voltages. Moreover, the charging processes are strongly influenced by CO_2 contamination, which can exhibit increased overvoltages and reduced capacity. Therefore, CO_2 poisoning has an adverse effect on the performance of metal-air batteries.

To resolve CO_2 poisoning on catalysts, tremendous efforts are focused on the design of air electrode catalysts that are resistive to CO_2 poisoning [102, 103]. Chen et al. [104] reported a double perovskite $PrBa_{0.8}Ca_{0.2}Co_2O_{5+d}$ (PBCC, Fig. 8a,b) catalyst with excellent ORR activity and remarkable CO_2 tolerance under realistic operating conditions. When tested in a solid oxide fuel cell in air with 1 vol% CO_2 at 750 ^oC, the PBCC electrode shows a specific areal resistance of 0.024 Ω cm^2, which further increases to 0.028 Ω cm^2 after 1000 h operation (Fig. 8c). The fast ORR kinetics and excellent durability of PBCC in the air with CO_2 are attributed to the surface of the PBCC electrode are much more active for oxygen exchange and more robust against CO_2 (Fig. 8d). Their study highlights the potential of PBCC as a highly promising material for metal-air batteries involving oxygen electrochemistry. Although this strategy can extend the life of the catalyst to some extent, it has not fundamentally

solved the problem of CO_2 poisoning. Therefore, how to solve the problem of CO_2 poisoning through catalyst design still needs further study.

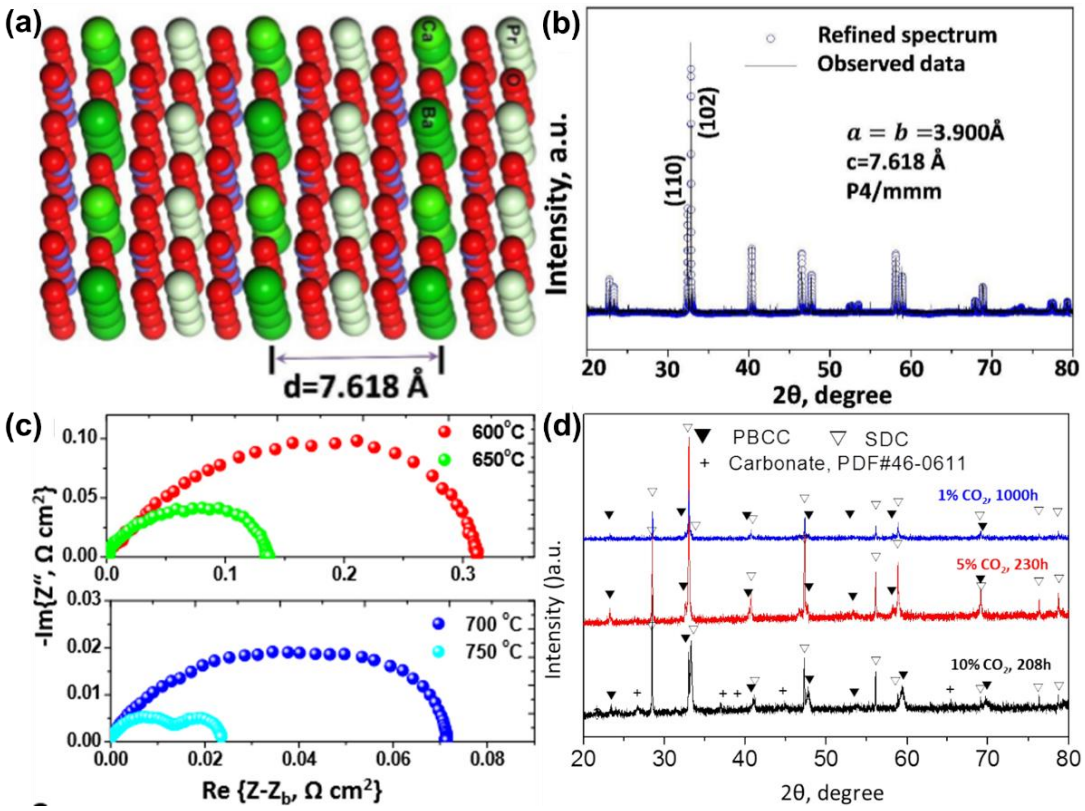

Fig. 8 (a) Schematics of the PBCC crystal structure. (b) Refined XRD profiles of PBCC (powder sample). (c) EIS of symmetrical cells with PBCC as an electrode in ambient air. (d) XRD patterns of PBCC cathode after testing with CO_2 concentration of 1% (green line), 5% (red line) and 10% (black line) [104]. Copyright 2018, Royal Society of Chemistry.

2.4.2. Water evaporation

In addition to CO_2 poisoning, water evaporation is another potential challenge of metal-air battery system [105]. In HSABs, only Na dissolution and precipitation occur on the anode, and no water is produced. The O_2 reduction and evolution reactions on

the air electrode will be accompanied by water reaction. In general, evaporation of aqueous electrolyte leading to membrane and catalyst layer dry out, resulting in an increase in resistive and activation losses [106, 107]. Although some water management techniques have shown the good results [108, 109], they all require bulky components such as humidifiers, blowers, compressors, and it is often accompanied by significant parasitic power loss [110]. To effectively prevent the water evaporation, a good design of air electrode interface is the key to regulating water management, which can not only inhibit the water evaporation, but also control the adsorption and release of oxygen.

Shen et al. [111] constructed an air diffusion electrode composed of the catalytic layer and nickel foam current collector. In the catalytic layer, reduced graphene-Co_3O_4 catalyst was mixed with polytetrafluoroethylene (PTFE, 60 wt.%) to produce a uniform membrane with a good interface. The air diffusion electrode displayed an overpotential of 1.6 V in the charge-discharge process after 100 cycles without water evaporation. In addition to PTFE, Nafion is also an effective additive for designing a good interface for air electrodes. Nguyen et al. [112] designed an air electrode structure that was composed of Nafion and Pt/carbon catalysts, in which the void space was partially filled with nano-sized hydrophobic particles Teflon (Fig. 9a). Such design not only enables efficient transport of proton and electron by Nafion and carbon materials, respectively, but also prevent the water evaporation owing to nano-sized hydrophobic particles Teflon at the interface of the air electrode. Alternatively, Fabian et al. [105] reported a water management design based on a hydrophilic and electrically conductive wick (Fig. 9b). Wilkinson et al. [113] proved that the characteristic knee in the polarization curve

is effectively removed by water management resulting in improved stability and performance reproducibility (Fig. 9c). Pasaogullari et al. [114] also reported that the discharge voltage and power density were both improved after a proper design of water management (Fig. 9d). The resulting inserted hydrophobic phase provides an independent gas transport path for the reactant gas, which prevents the impairment of gas transport by water evaporation in the catalytic layer of the air electrode.

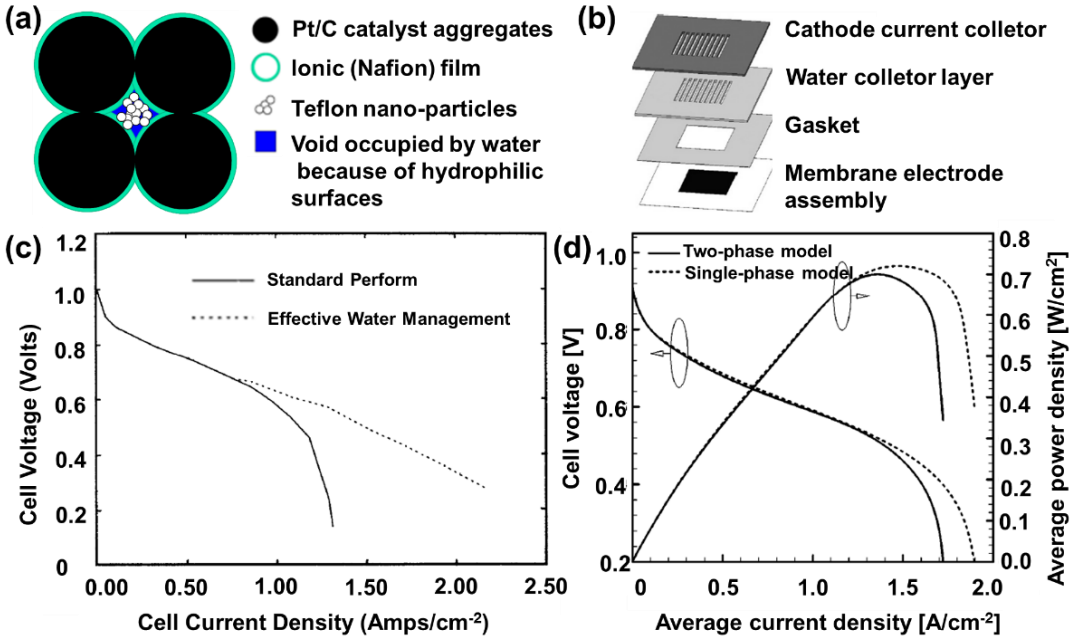

Fig. 9 (a) Distribution of an ideal four-phase (electronic-ionic-gas-liquid) catalyst layer structure [112]. Copyright 2006, ECS. (b) Exploded view of the air-breathing fuel cell cathode comprising active area membrane electrode assembly, gasket, in-plane water collector, and cathode current collector [105]. Copyright 2010, Elsevier. (c) Polarization curves for a single cell with and without effective water management (232 cm^2 active area, Dow XUS-13204.10 membrane, P_{H2} =Pair =4.5 bar, T_{cell}=70 ºC) [113]. Copyright 1994, Elsevier. (d) Calculated polarization and power curves of two-channel serpentine

polymer electrolyte fuel cell at a cell temperature of 80 °C, inlet pressures of 1.5 atm, fully humidified inlets at 80 °C, and anode/cathode stoichiometry: 2 at 1 A/cm^2 [114]. Copyright 2005, ECS.

3. Catalyst design for air electrodes

In metal-air batteries, the introduction of various catalysts into the air electrode is an effective strategy for improving the reversibility and electrochemical performance of HSABs. Generally, the catalysts used in metal-air batteries should possess the following factors [115]: (1) a highly conductive and porous catalyst substrate to ensure high electron conductivity and rapid liquid/gas transportation; (2) nanostructured catalyst particles to increase catalyst utilization; (3) abundant and well-dispersed catalyst sites to improve OER/ORR kinetics; and (4) environmentally benign properties of the chemical composition of the catalyst. With the development of air electrode catalysts, the requirement for the amount of active sites on the surface of catalysts is becoming higher and higher. Here, we discuss the recent process of air electrode catalysts based on different metal-air batteries to provide theoretical guidance for the design of air electrode catalysts in HSABs according to the features of various catalysts. Furthermore, some important synthesis approaches are reviewed to guide the preparation of the desired catalysts.

3.1. Classification

3.1.1. Carbon-based catalyst

ORR is the critical step for determining the performance of various next-generation metal-air energy storage devices [116]. Pt-based electrocatalysts exhibit superior overall performance for ORR; however, the high cost and low natural abundance of Pt limit the large-scale commercialization of metal-air energy storage devices [117, 118]. In this context, doped carbon materials, such as graphene, carbon nanotubes (CNTs), carbon nanofibers (CNFs), microporous carbon sheets, and carbon aerogels are effective electrocatalysts for ORR [119, 120]. Heteroatoms, such as O [121], N [122], P [123], B [124], and S [125] have been demonstrated to alter the electronic properties of carbon frameworks and their adsorption/desorption behavior towards oxygen intermediates, thus providing additional ORR active sites and promoting the electrocatalytic kinetic processes of oxygen [126].

Ma et al. [127] activated and stabilized N-doped carbon fiber air electrode by in-situ Co embedding/coating. In Na-O_2 battery, the air electrode exhibited superior electrochemical performance, showing low charge overpotential, high specific capacity, and satisfactory cycle stability. These features can be attributed to the combined advantages associated with electron and mass transportation, which are facilitated by the fiber shape, binder-free and porous structure of the air electrode. Furthermore, the air electrode exhibited high conductivity and catalytic activity, which are attributed to the synergy between N-doped carbon fibers and partially oxidized Co, as well as the successful tailor of the morphology of discharge products.

Luo et al. [128] reported a self-terminated activation strategy for the high-yield production of nitrogen and phosphorus co-doped nanoporous carbon (NP-NC) by using

potassium phytate as a carbonaceous source (Fig. 10a). Benefiting from the high surface area of 1294 m^2 g^{-1} and trimodal nanoporous structure, the resulting N, P-co-doped catalyst exhibited excellent ORR activity that was close to that of Pt/C, high catalytic current density, excellent methanol tolerance, and durability. As a cathode catalyst for ZABs, NP-NC exhibits current and power densities that are comparable to those of state-of-the-art 20% Pt/C. Chandrasekaran et al. [129] obtained N- and S-doped porous carbon monoliths by subjecting polyisocyanurate gels to thermal treatment at 1000 °C with elemental sulfur under inert conditions. The optimized sulfur concentration (5.6 wt%) into the carbon matrix displayed excellent oxygen reduction activity with direct four-electron transfer relative to its pristine counterparts by providing more –C–S–C– active species with additional oxygen adsorption sites than oxidized sulfur species (Fig. 10b, c). It has been reported that N-doping can promote electron donation from the catalyst to the O_2 molecule, thus facilitating ORR [130]. When a P site is oxidized and bound to an N co-dopant, it stabilizes the graphitic N and activates a neighboring C site for effective OER. Therefore, P and N co-doped carbons show bifunctional ORR and OER activities [131].

Wang et al. [132] demonstrated a non-polluting fabrication of porous carbon self-doped with N and P heteroatoms from spirulina that is an industrially cultivated microalgae that is rich in proteins and phosphates. The N, P self-doped biocarbon (NPBC) exhibited large specific surface area (786.1 m^2 g^{-1}), improved pore volume (0.73 cm^3 g^{-1}), and doping levels of 2.15 at.% for N and 0.97 at.% for P. Furthermore, such biocarbon can deliver bifunctional activity in catalyzing ORR and OER (Fig. 10d).

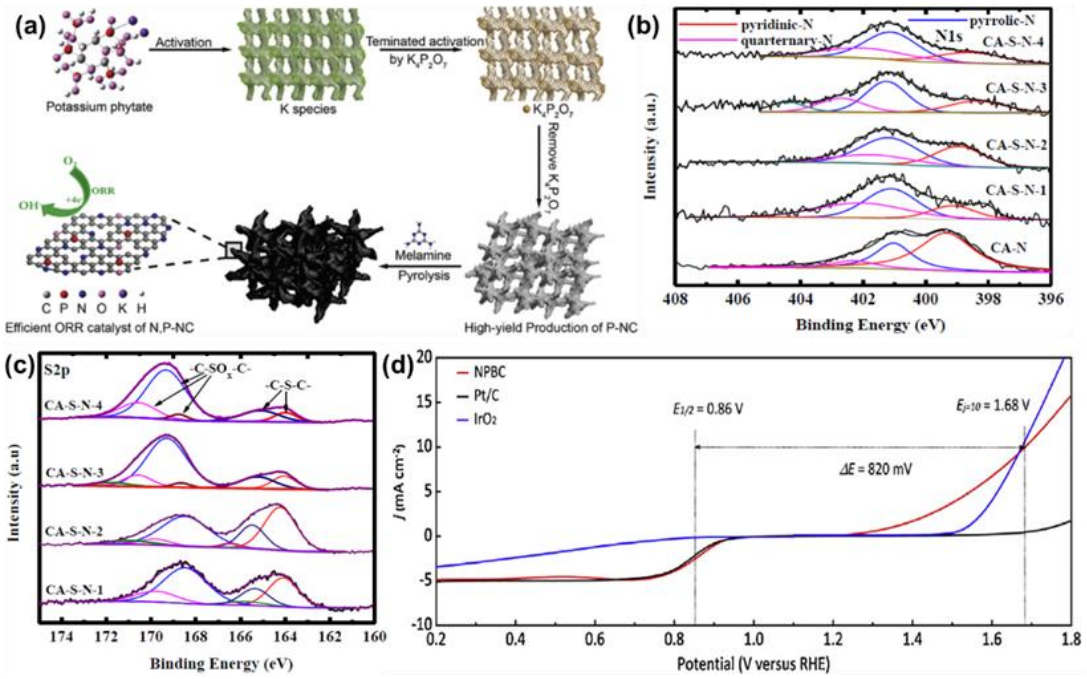

Fig. 10 (a) Schematic of NP-NC electrocatalyst preparation [128]. Copyright 2018, Elsevier. (b) High-resolution N1s spectra and (c) high-resolution S2p spectra of S, N-doped carbon [129]. Copyright 2018, American Chemical Society. (d) ORR and OER polarization curves of NPBC, Pt/C, and IrO_2/C in 0.1 mol L^{-1} KOH solution [130]. Copyright 2017, Elsevier.

Heteroatom-doped carbon materials have been explored as alternative efficient ORR catalysts and are expected to replace the traditional Pt-based catalyst electrode. Generally, element doping, such as N, P, B, S, etc., can further improve the ORR performances in metal-air batteries due to the modification of surface structure, electronic properties, and adsorption/desorption behaviors towards oxygen intermediates. Especially, N and P elements lead to superior catalytic activity for ORR due to prominent modification of the specific surface area and pore volume of carbon

materials. However, the fact that carbon material catalysts are easily oxidized to carbon oxides during charging, showing the instability and shortcomings of carbon-based catalysts [133, 134].

3.1.2. Metal-based catalyst

Metal-based catalysts are rising for energy conversion and energy storage devices owing to their superior OER performance and satisfactory cycle performance [135]. Materials based on precious metals, such as Ru and Ir [136, 137], and transition metals (Co and Fe) have been developed as OER catalysts for metal-air batteries [138–140]. Noble metal (Pd, Pt, Ru, and Au) and some metal alloys (Pt_3Co and Pd_3Co) as catalysts have shown satisfactory electrochemical properties, which can improve the cyclability and reduce the large overpotential [141–144]. Cho et al. [144] reported that a LAB cell employed with Pd_3Co/KetjenBlack EC600JD (KB) as electrocatalyst exhibits a charging overpotential of 4.2 V, which is 200 mV lower than that of a LAB cell with a typical MnO_2/KB electrocatalyst. In addition, Pd_3Co/KB exhibited excellent cyclability (1000 mAh g^{-1}) for 35 cycles.

To improve its ORR performance, Fu et al. [145] modified the metal catalyst by carbon materials and synthesized Ni_3Fe nanoparticles (NPs) embedded in N-doped porous graphitic carbon sheets (Ni_3Fe/N-C sheets, Fig. 11a–11c). They demonstrated that the Ni_3Fe/N-C sheets possess improved ORR and OER performance. Composites can be stabilized by embedding Ni_3Fe NPs within graphitic carbon sheets. The stabilized composites exhibit long-term cycling stability. Yui et al. [146] prepared

$Pt_{100-x}Ru_x$ ($0 \leq x \leq 100$) electrocatalysts through the formic acid reduction method. The prepared air electrodes were examined in 1 mol L^{-1} LiTFSA/TEGDME electrolyte solution (Fig. 11d). Among the studied samples, the optimized $Pt_{10}Ru_{90}$/carbon sample showed the largest discharge capacity (1014 mAh g^{-1}) and the lowest average charge voltage (3.74 V). The optimized sample exhibited comparatively decent cycle stability with a discharge capacity of over 800 mAh g^{-1} at the 8th cycle. Wang et al. [147] developed graphene nanosheets functionalized with monodispersed Ru (101) NPs with an average size of 2 nm (Fig. 11e). A low charge voltage of 4.02 V with a high Coulombic efficiency of 89.2% and a satisfactory cycle stability with 500 mAh g^{-1} capacity retained at 67 cycles were achieved in LABs (Figs. 11f and 11g).

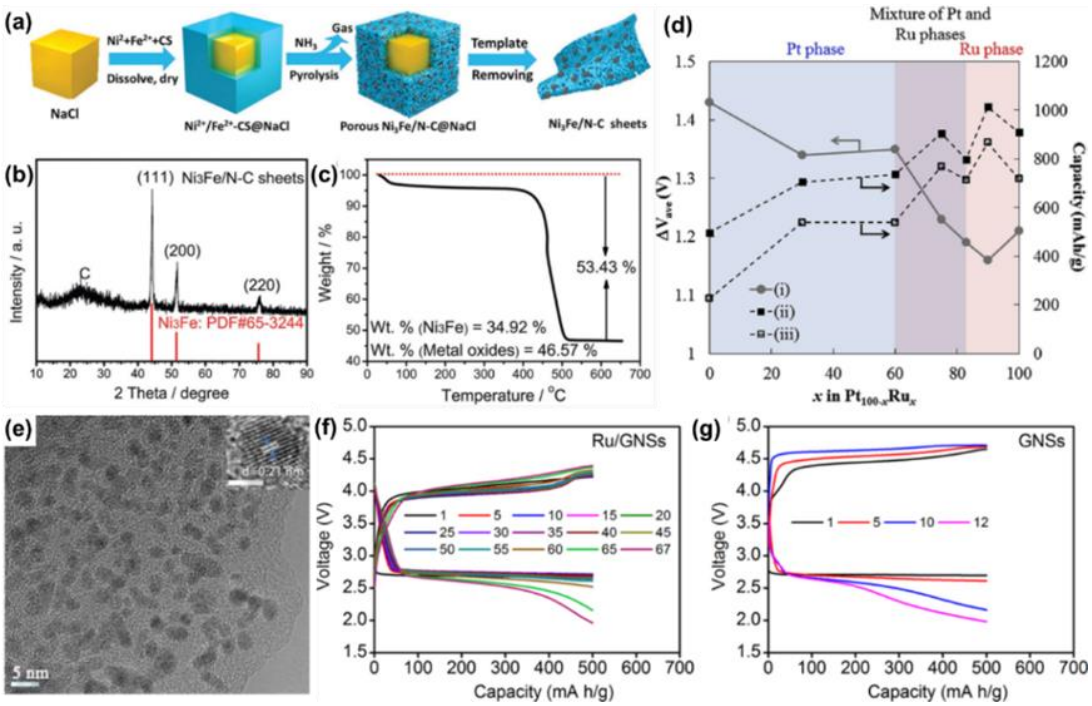

Fig. 11 (a) Schematic of the formation of Ni_3Fe/N-C sheets. (b) XRD pattern and (c) TGA curve of the Ni_3Fe/N-C sheets [145]. Copyright 2017, Wiley. (d) ΔV_{ave} and discharge/charge capacity for LAB cells incorporating air electrodes loaded with

various composition ratios of $Pt_{100-x}Ru_x$/KB: (i) ΔV_{ave}, (ii) discharge capacity, and (iii) charge capacity [146]. Copyright 2017, Elesiver. (e) TEM images of Ru/GNSs. The inset is the corresponding HRTEM image of a single Ru particle with the white scale bar of 2 nm. Cycling performance of (f) Ru/GNSs and (g) GNSs cathodes in CO_2 with 2% O_2 atmosphere at a limited capacity of 500 mAh g^{-1} [147]. Copyright 2017, American Chemical Society.

Thus far, metal-based materials have emerged as promising electrocatalysts with highly active and stable OER electrocatalytic performance owing to the decent Coulombic efficiency, cycle stability, and low overpotential in metal-air batteries. Although the ORR performance of the metal-based catalyst/carbon composites is enhanced, its synthesis requires complex procedures, such as hydrothermal methods and subsequent high-temperature annealing treatment. A simple, large-scale, and low-cost synthetic approach for the fabrication of these catalysts is needed to develop.

3.1.3. Metal oxide-based catalyst

As a class of bifunctional ORR and OER catalysts, metal oxides are extensively studied because of their high activity, stability, and low-cost in alkaline solutions for metal-air batteries [148–150]. Moreover, the electrochemical activity of transition metal oxides can be improved by altering their compositions, crystal structures, and morphologies [151]. In particular, the bifunctional properties of binary transition metal oxides are easier to achieve. Mohamed et al. [152] fabricated ternary spinel $FeCo_2O_4$

porous nanorods as a bifunctional catalyst for Li-O_2 batteries. The active sites of the materials easily adsorbed oxygen because of the extreme high Co^{3+} content on the $FeCo_2O_4$ surface; exhibiting low overpotential and high capacity. Xu et al. [153] designed and synthesized the $CoFe_2O_4$@CNTs nanoparticles as bifunctional catalysts for rechargeable zinc-air batteries, exhibiting high power density (333.7 mW cm^{-2}), high specific capacity (732 mAh g^{-1}), and good rechargeability (1200 stable charge-discharge cycles). The enhanced performance of the ZABs is attributed to CNTs exhibiting efficient ORR and the crystalline structure of $CoFe_2O_4$ is beneficial for OER.

Reducing the dimension of catalysts is an important strategy for improving the bifunctional properties of catalysts. Ryu et al. [154] proposed a high-aspect ratio 1D Co_3O_4 nanofiber as bifunctional composite catalysts for Li-O_2 batteries with large capacities and stable cycle. The battery exhibits a high first discharge capacity of 10 500 mAh g^{-1} and superior cyclability for 80 cycles with a limited capacity of 1000 mAh g^{-1} owing to the large surface area, facile electron transport, and rapid O_2 diffusion.

Yin et al. [155] utilized liquid redox mediators to control the morphology of the discharged products in SABs. When Co_3O_4 nanowires were used as air electrodes, the discharge product tended to be nanoflake-like properties. However, after the addition of ferrocene to the electrolyte, the discharge product tended to behave like nanofilms, and the battery can reach 570 cycles. Hu et al. [156] used MnO_2 nanocomposite catalyst integrated with N,N′-bis(salicylidene)ethylene diaminocobalt (II) (CoII-salen) in the electrolyte for LABs. Such combination has two advantages: (1) the coating layer of δ-MnO_2 on the MnO_2 nanocomposite catalyzes Li_2O_2 decomposition and suppresses side

reactions, and (2) CoII-salen works as a mobile O_2-carrier and accelerates Li_2O_2 formation through the reaction of CoIII-salen (Fig. 12a). LAB with a Co-salen/MnO_2 catalyst displayed a discharge capacity of 18 100 mAh g^{-1} with a mean discharge voltage of 2.8 V and a capacity of 1000 mAh g^{-1} after 300 cycles at 500 mA g^{-1} (0.15 mA cm^{-2}; Fig. 12b). Zhang et al. [157] reported a bifunctional catalyst of ruthenium dioxide (RuO_2)-decorated carbonized tubular polypyrrole (CTPPy) with two special features: (1) a high content of graphitic N and (2) a large number of RuO_2 NPs (Fig. 12c). The battery delivered a large discharge capacity of 10 095 mAh g^{-1} at a current density of 200 mA g^{-1}, a high rate capacity of 6758 mAh g^{-1} at a current density of 1000 mA g^{-1}, and long cycling life of 55 cycles at a current density of 500 mA g^{-1}. Cheng et al. [158] designed ultrafine NiFeO NPs in a porous amorphous MnO_x layer. The NiFeO-core contributed to the high activity for the OER, and the amorphous MnO_x shell was an active phase for the ORR, signifying the synergistic effect of the NiFeO core and MnO_x shell (Fig. 12d). The synergistic effect is related to the electron drawing of the NiFeO core from the MnO_x shell, decreasing the affinity and adsorption energy of oxygen on the MnO_x shell and substantially increasing the ORR kinetics.

Compared to carbon- and metal-based catalysts, metal oxide catalysts endow bifunctionality for ORR and OER. The electrocatalytic activity of metal oxide-based catalysts can be enhanced by tailoring the crystal structure and the morphology. Although metal oxides have good ORR and OER properties, they usually exhibit poor conductivity in batteries. Rational design of air electrode composed of desirable metal oxides and carbon materials could significantly improve the electrocatalytic activity

and further extend the cycle life of metal-air batteries, which is an emerging area for future research.

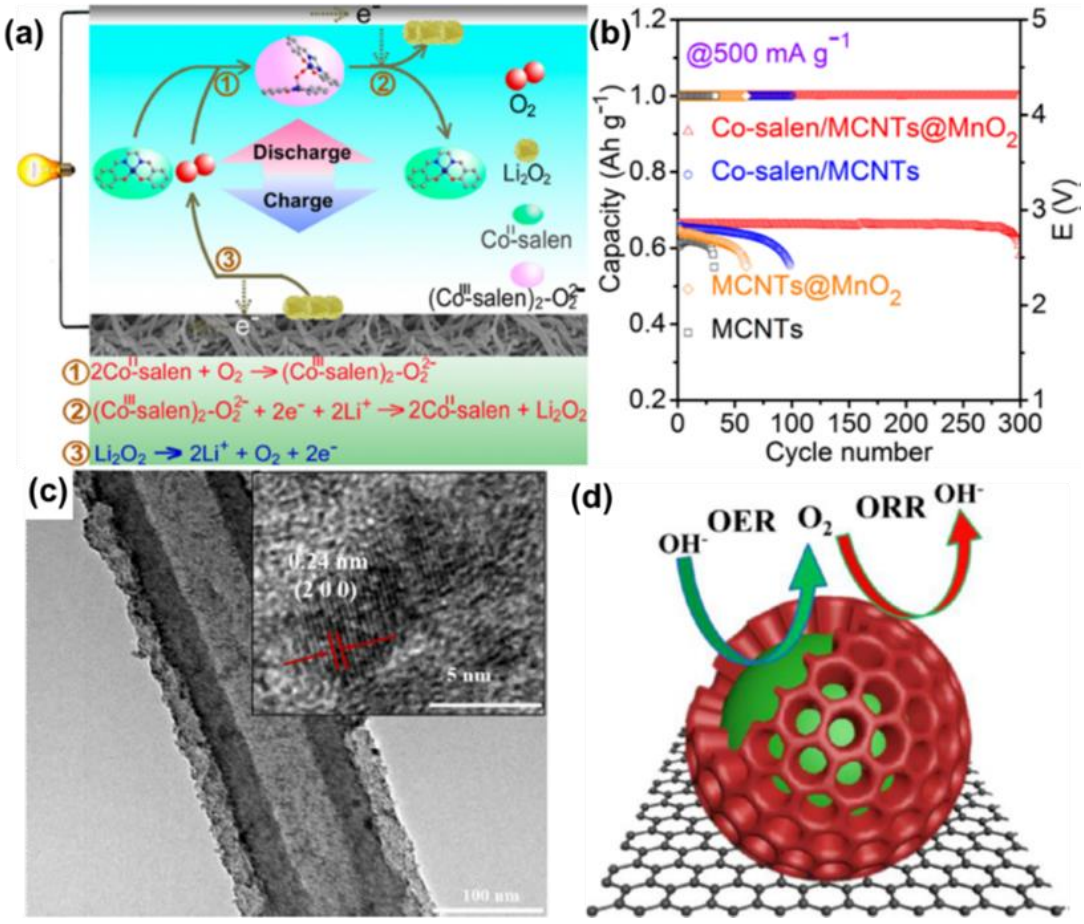

Fig. 12 (a) Schematic and reaction mechanism of the LABs with CoII-salen in the electrolyte during discharge and charge process. (b) Cyclability comparison with the controlled capacity of 1000 mAh g^{-1} (0.30 mAh cm^{-2}) at 500 mA g^{-1} (0.15 mA cm^{-2}) [156]. Copyright 2017, American Chemical Society. (c) TEM image of RuO_2-decorated CTPPy. The inset represents the lattice fringes of RuO_2 nanoparticle [157]. Copyright 2017, Elsevier. (d) Scheme showing the bifunctional activity and structural confinement of NiFeO@MnOx core−shell structured catalysts for OER and ORR [158]. Copyright 2017, American Chemical Society.

3.1.4. Perovskite-based catalysts

Among bifunctional catalysts, perovskite oxides have high ionic/electronic conductivity. It can solve the problem of insufficient conductivity of metal oxides. Moreover, compared to traditional metal oxides, the specific structure of perovskite oxides can provide rich oxygen vacancies because the ABO_3 structure allows elemental substitution at A and/or B sites over a wide composition range [159]. These perovskite oxides possess desirable catalytic performance without the need of carbon hosts owing to the ease of crystal structure adjustment and reversal of crystal defects [160]. Oxygen vacancies can enhance the transfer of oxygen ions, and the optimized chemical composition can improve ORR and OER performance [161, 162]. The abovementioned characteristics make them highly suitable for metal-air batteries.

Sunarso et al. [163] illustrated that $LaCoO_3$ exhibited enhanced catalytic activity and rechargeable stability for metal-air batteries. Xu et al. [164] prepared porous $La_{0.75}Sr_{0.25}MnO_3$ nanotubes with high surface areas through electrospinning. $La_{0.75}Sr_{0.25}MnO_3$ nanotubes prolong the cycling life and lower the overvoltage of lithium-oxygen batteries.

Xue et al. [165] synthesized strontium-doped $(La_{1-x}Sr_x)_{0.98}MnO_3$ (LSM, x = 0.2–0.5) perovskites with the A-site deficiencies, Mn valence and the O species by a modified solid-liquid method. The AAB with 50% LSM exhibited the power density of 191.3 mW cm^{-2}. Gong et al. [166] proposed that perovskite $LaNiO_3$ is an efficient bifunctional catalyst for OER and ORR. They showed that $LaNiO_3$ display substantially

reduced discharge/charge voltage gap of 0.77 V at 50 mA g^{-1} with decent rate capability and considerable cycle stability.

The catalytic activity of perovskite can be further improved by controlling the electronic structure of perovskite via element doping. Bu et al. [167] prepared mesoporous (5-10 nm) nanofibers (300 nm) of various cation-ordered $PrBa_{0.5}Sr_{0.5}Co_{2-x}Fe_xO_{5+\delta}$ (x = 0, 0.5, 1, 1.5, and 2) perovskites via electrospinning. The synthesized $PrBa_{0.5}Sr_{0.5}Co_{2-x}Fe_xO_{5+\delta}$ possesses tetragonal (P4/mmm) structure with lattice parameters of a = 3.871 Å and c = 7.757 Å (Fig. 13a and Fig. 13b). The well-controlled B-site metal ratio and large surface area (~20 m^2 g^{-1}) of the mesoporous nanofiber result in high performance of the ORR and OER and stability in ZABs. Zhao et al. [168] prepared Sr-doped perovskite oxides $La_{1-x}Sr_xMnO_3$ (x = 0, 0.2, 0.6) catalysts for the oxygen cathode in rechargeable LABs. These oxides possessed higher catalytic activities than that of the pure $LaMnO_3$ (Fig. 13c). $La_{0.4}Sr_{0.6}MnO_3$ had a lower overpotential between the OER and ORR than $La_{0.8}Sr_{0.2}MnO_3$ and $LaMnO_3$ (Figs. 13d–13f). The cell with $La_{0.4}Sr_{0.6}MnO_3$ as the catalyst can be cycled at a limited capacity of 200 mAh g^{-1} for 71 cycles. Although perovskite materials have exhibited desirable bifunctional catalytic activities and good conductivity, it is well known that the structural stability of perovskite has been the biggest obstacle to its application, which seriously affects the cycle performance of HSABs.

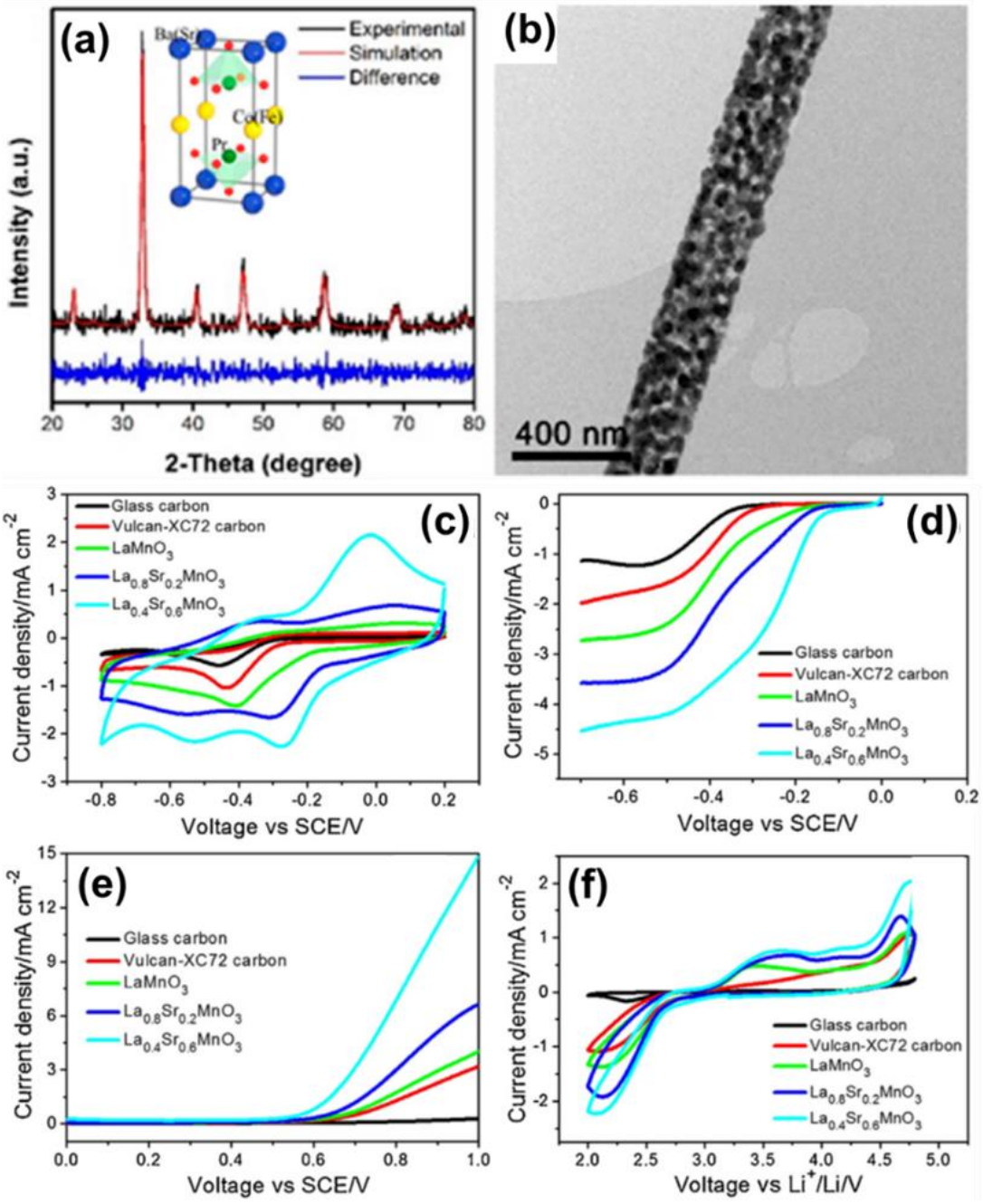

Fig. 13 (a) Refined XRD profiles of the $PrBa_{0.5}Sr_{0.5}Co_{2-x}Fe_xO_{5+\delta}$ nanofiber (PBSCF-NF). (b) TEM image of the PBSCF-NF [167]. Copyright 2017, American Chemical Society. (c) Cyclic voltammograms of glassy carbon, VC, and $La_{1-x}SrxMnO_3$ (x = 0, 0.2, 0.6) tested in O_2-saturated 0.1 mol L^{-1} KOH solution at 50 mV s^{-1}. (d) ORR (negative scan) polarization profiles of glassy carbon, VC, $La_{1-x}Sr_xMnO_3$ (x = 0, 0.2, 0.6), and Pt/C at 1600 rpm and 10 mV s^{-1} in O_2-saturated 0.1 mol L^{-1} KOH solution.

(e) OER (positive scan) polarization profiles of glassy carbon, VC, $La_{1-x}Sr_xMnO_3$ (x = 0, 0.2, 0.6), and Pt/C at 1600 rpm. (f) Cyclic voltammograms of glassy carbon, VC, and $La_{1-x}Sr_xMnO_3$ (x = 0, 0.2, 0.6) within a potential window of 2–4.8 vs Li^+/Li/V in O_2-saturated electrolyte containing 1 mol L^{-1} $LiCF_3SO_3$ in TEGDME at a scan rate of 10 mV s^{-1} and a rotating rate of 900 rpm [168]. Copyright 2017, Elsevier.

3.1.5. Metal-organic framework-based catalyst

Recently, metal-organic frameworks (MOFs) have attracted increasing attention because of their fascinating architectures and excellent pore properties [169]. Previous research demonstrated the application of MOFs as precursors for the synthesis of porous carbon and metal oxides for gas storage and energy conversion and storage [170–172]. MOF-derived nanostructured materials are promising bifunctional electrocatalysts owing to their large specific surface area, robust morphology, and porosity [173]. Li et al. [174] fabricated an N-doped Fe/Fe_3C@graphitic layer/CNT hybrid derived from MOFs. This hybrid exhibited outstanding bifunctional electrocatalytic activity for ORR and OER due to the graphitic layer/CNT structures with highly active N and Fe/Fe_3C sites. The performance of MOFs derivatives can be further improved by controlling their composition and structure. Zhu et al. [175] reported an innovative approach for synthesizing N and S co-doped honeycomb-like porous carbon immobilizing Co_9S_8 NPs using an Al-based MOF (MIL-101-NH2), resulting in highly efficient catalytic activity for ORR and high durability under alkaline conditions. Dou et al. [176] prepared a highly efficient bifunctional electrocatalyst Co-

embedded CNT/porous carbon (originated from ZIF-67) toward the ORR and OER. It showed satisfactory cycling stabilities in the ZAB at 2 mA cm^{-2} after 100 cycles and the potential attenuations of the ORR and OER are lower than 10%.

Qian et al. [177] synthesized dual-doped and metal-free porous carbon materials with high specific surface areas as efficient ORR/OER bifunctional electrocatalysts by pyrolyzing a MOF containing Zn, N, and B (Fig. 14a). The resultant carbon materials exhibited high ORR and OER catalytic activities. This finding indicated that MOFs could be used as precursors for the synthesis of metal-free ORR/OER bifunctional cathodic electrocatalysts with excellent potential in rechargeable ZABs. Li et al. [178] synthesized N, P-containing MOF coated on CNTs as high-performance catalysts (Fig. 14b). The MOF coating played essential roles in (1) accelerating mass and charge transfer, (2) promoting ORR activity, and (3) facilitating the formation of numerous catalytic active sites on the CNTs, which exhibited improved stability that is comparable to that of Pt/C cathode for ZABs. In addition, another advantage of MOFs-based catalysts is that their composition and structure can be designed according to requirements. Liu et al. [179] synthesized an rGO-supported $ZnO/ZnCo_2O_4$ NP-embedded carbon hollow nanocage ($ZnO/ZnCo_2O_4$/C@rGO) hybrid by using a ZIF-67/GO/zinc nitrate composite as the precursor (Fig. 14c). The nanocomposite material exhibited excellent electrocatalytic activity toward ORR and superior stability under alkaline conditions. Abirami et al. [56] applied MOF-derived porous Co manganese oxide (CMO) nanocubes as efficient bifunctional electrocatalysts in rechargeable seawater HSABs (Fig. 14d). The improved performance was due to the large surface

areas and high oxidation states of the randomly distributed Co and Mn cations in the CMO nanocubes (Fig. 14e).

MOF-based catalysts can be efficient bifunctional electrocatalysts owing to their high specific surface areas and porosities, which can be easily controlled by optimizing the thermal annealing treatment [180, 181]. To further enhance the electrocatalytic performance of MOF-based catalysts, further research can be conducted to optimize the porosity of MOF-derived carbon host. However, MOF-based catalysts also face some shortcomings, such as the complex synthesis process, high cost, low yield of the prepared catalyst from the MOF precursors. Therefore, the exploration of simple, large-scale, and cost-effective approach to synthesize desirable MOF-based bifunctional catalysts is necessary for the development of high-performance HSABs.

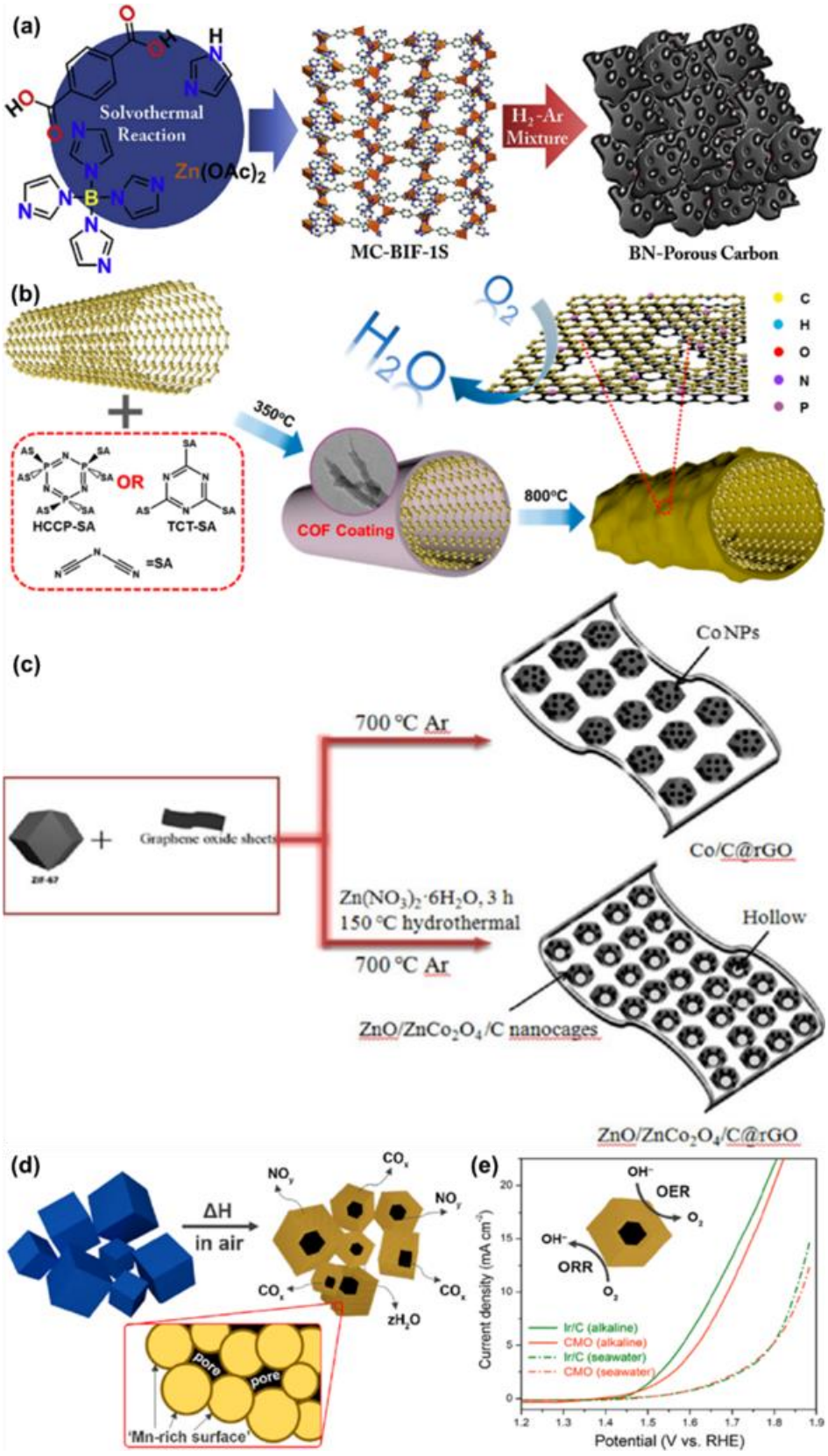

Fig. 14 (a) Synthetic scheme of BNPCs [177]. Copyright 2017, Elesiver. (b) Illustration of N,P-C preparation [178]. Copyright 2017, American Chemical Society. (c)

Schematic of the synthesis of Co/C@rGO and ZnO/$ZnCo_2O_4$/C@rGO hybrids [179]. Copyright 2017, American Chemical Society. (d) Schematic of the morphological evolution of porous CMO nanocubes by air annealing. (e) Anodic polarization curves for the OER measured in 0.1 M NaOH (solid) and seawater (dash) of the CMO catalyst compared to 20 wt.% Ir/C [56]. Copyright 2016, American Chemical Society.

3.1.6. Single-atom catalyst

The cost and efficiency of catalysts are crucial factors for practical applications. For this purpose, single-atom catalysts (SACs) may be a breakthrough point in the electrocatalysis community due to their outstanding advantage of maximum atom utilization efficiency [182]. Early to 1990s, the first preparation of SACs was reported based on silica-supported zirconium and tantalum complexes by Lecuyer's group [183]. SACs supported carbon materials are becoming one of the most promising candidates [184, 185]. For example, carbon materials have good electrical conductivity and provide anchoring sites for SACs, manipulating the charge density and electronic structure of the metal atoms due to strong interfacial interactions of metal atoms and carbon atoms [186]. Recently, SACs of some transition metals such as iron, cobalt and nickel, supported on carbon substrates have emerged as a promising and low-cost electrocatalysts because of maximal atom utilization (≈100%) and high efficiency for a range of reactions involved in electrochemical energy conversion and storage, such as the oxygen reduction, oxygen evolution, etc [186]. Such attributes may be exploited for the enhancement of the electrocatalytic performance due to the lower binding energy

caused by shorter bond length. Chen et al. [187] designed the atomically dispersed iron-nitrogen sites supported on hierarchical carbon nanotubes co-decorated with nitrogen and sulfur (S,N-Fe/N/C-CNT) for ZABs(Fig. 15a). The polarization curve of the S,N-Fe/N/C-CNT catalyst exhibited a small overpotential of 370 mV at a current density of 10 mA cm^2 (Fig. 15b), having a half-wave potential of 0.85 V (Pt/C=0.82 V). A high limiting current density of 6.68 $mAcm^{-2}$ was obtained at a potential of 0.2 V (Fig. 15c). Han et al. [188] performed aberration-corrected high angle annular dark-field scanning transmission electron microscopy (AC-HAADF-STEM) measurements to elucidate the existing form of isolated cobalt atoms anchored on hollow N-doped carbon spheres (ISAS-Co/ HNCS, Fig. 15d).

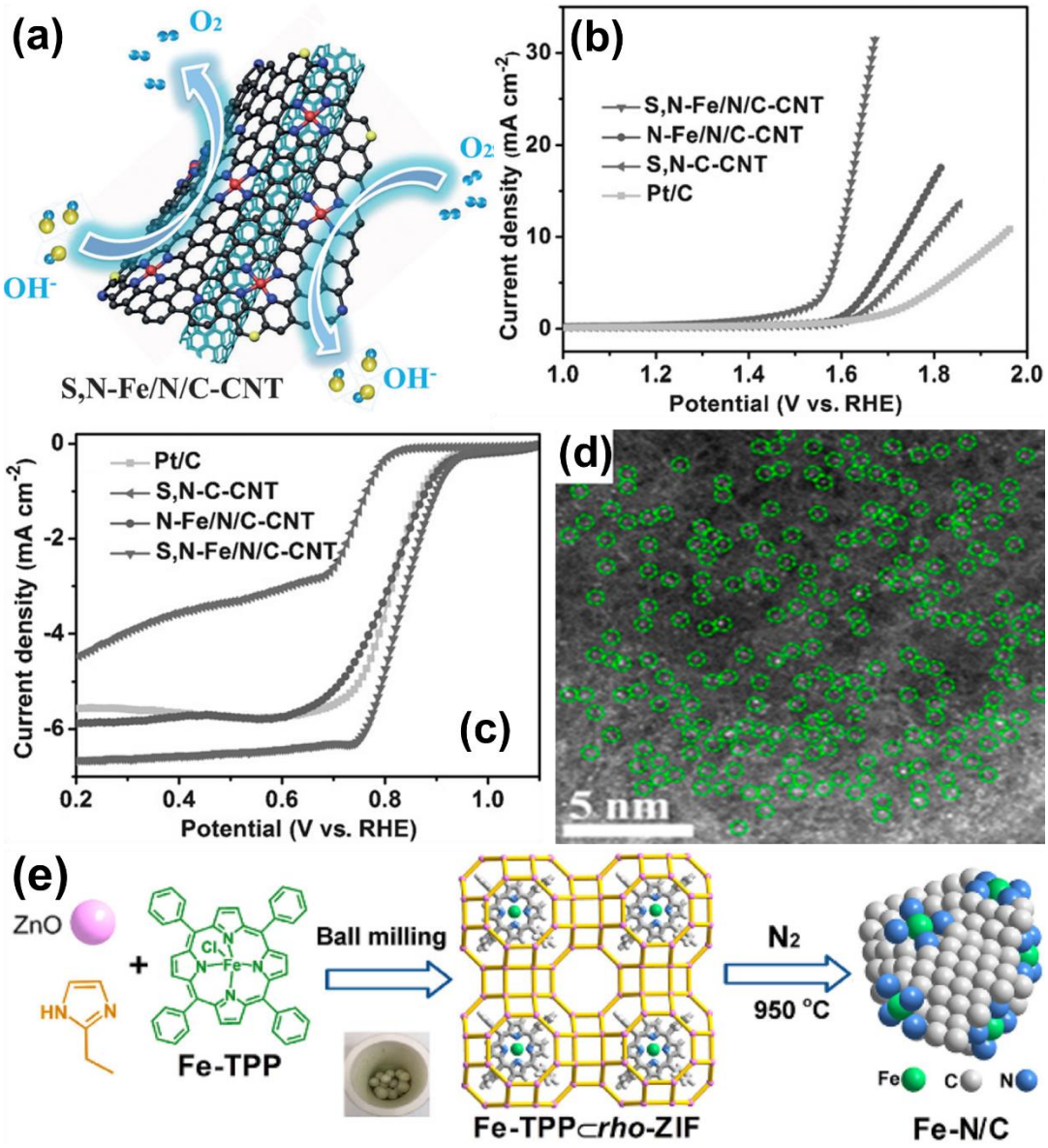

Fig. 15 (a) Scheme for S,N-Fe/N/C-CNT, (b) IR-corrected OER polarization curves, and (c) ORR polarization curves of S,N-Fe/N/C-CNT, N-Fe/ N/C-CNT, S,N-C-CNT samples, and commercial Pt/C, in 0.1m KOH solution [187]. Copyright 2016, Wiley. (d) AC HAADF-STEM image of ISAS-Co/HNCS; isolated bright dots marked with light-green circles are cobalt atoms [188]. Copyright 2017, American Chemical Society. (e) The schematic illustration for the non-solution fabrication process of Fe-N/C [189]. Copyright 2018, Elsevier.

Very recently, Xu et al. [190] reported a rational design of highly efficient and cost-effective SACs, revealing that the local structural and chemical environment of the active centers can serve as a universal descriptor to predict the ORR and OER activities. Zhu et al. [191] synthesized the Fe–N-doped carbon nanotube aerogels (Fe-N-CNTAs) using tellurium nanowires as hard templates in the presence of nitrogen-containing small molecule and inorganic salt for ZABs. It showed high ORR activity and much better stability than the Pt/C catalysts in alkaline medium. Shen et al. [192] synthesized a sulfur-doped Fe/N/C electrocatalyst (Fe/SNC) by a template casting method to produce high-density atomically dispersed Fe@N@C sites that outperforms commercial Pt/C for the ORR in alkaline solutions. The Fe/SNC catalyst has a high half-wave potential of 0.77 V and Pt/C-comparable stability. Especially, MOFs have been extensively used as a template to synthesize SACs [189, 193, 194]. Wei et al. [189] prepared a new precursor of host-guest Fe-TPP⊂rho-ZIF (FeTPP = tetraphenylporphyrin iron; rho-ZIF = zeolitic imidazolate framework with the rho topology) by the one-pot mechanochemical method, that was pyrolyzed into Fe-N/C SACs for ZABs (Fig. 15e). The catalyst showed high ORR activity, good methanol tolerance and high durability. These studies concluded that low-cost SACs are undoubtedly the potential catalyst for air electrode in metal-air batteries because of their high utilization rate and catalytic performance [194-196].

3.1.7. Others

In addition to carbon-based, metal-based, transition metal oxide-based, perovskite-based, MOF-based catalysts and SACs, molybdenum sulfides (MoS_2) and their composite materials have been demonstrated as an effective catalyst for metal-air batteries. As a representative layered structure of 2D S−Mo−S layers, MoS_2 presents exotic structure-property relationship in wide applications, such as transistors, electrochemical hydrogen storage, and batteries [197]. Nevertheless, one of the key challenges associated with MoS_2 materials is the sluggish reaction kinetics, which restricts active material utilization [198]. Several approaches have been exploited to enhance the electrocatalytic activity of MoS_2 by controlling its atomic composition.

Zhang et al. [199] reported a novel and effective strategy to distort the lattice structure by constructing a metastable MoSSe solid solution and tune its catalytic activity. When evaluated as an oxygen electrode for deep-cycle Li−O_2 batteries, the metastable MoSSe solid solution delivered a high specific capacity of ~730 mAh g^{-1} with stable discharge−charge overpotential of 0.49 V in 30 cycles. Cui et al. [200] demonstrated a novel and highly efficient bimetallic carbide-based bifunctional catalyst, consisting of iron-molybdenum carbide (Fe_3Mo_3C) and IrMn nanoalloys. Fe_3Mo_3C acts as a highly efficient electrocatalyst for ORR and robust support that is chemically stable in alkaline media and over the potential range for ORR and OER. ZABs with IrMn/Fe_3Mo_3C air electrode exhibits long-term cycling performance of over 200 h with high efficiency (56.1%).

3.2. Preparation approaches

3.2.1. Wet-chemistry method

Numerous electrocatalysts have been produced for metal-air batteries through various synthesis methods, such as the hydrothermal method [201], solvothermal method [202], sol-gel method [203], precipitation method [204], template method [205], and the combination of these methods [204, 207]. These methods offer different advantages. For instance, the hydrothermal method provides an effective means to control catalyst morphology, whereas the sol-gel process can obtain homogeneous powder catalysts. The precipitation method offers the scale-up capability to prepare simple and controllable features. The template method can tailor advanced structures to meet the requirements. Examples of traditionally synthesized catalysts are highlighted to provide technical guidance for the synthesis of HSAB catalysts.

Hu et al. [208] synthesized perovskite $LaMnO_3$ nanorod/reduced graphene oxides (LMO-NR/RGO) through a simple hydrothermal reaction (Fig. 16a), and Ag-decorated LMO-NR/RGO composites were obtained through a traditional silver mirror reaction. Ag/LMO-NR/RGO acted as an effective catalyst for ORR and OER in an alkaline medium with enhanced electrochemical durability owing to the synergistic effect of the three components. Using the sol-gel method, Park et al. [209] presented highly pure single crystalline pyrochlore NPs with metallic conduction ($Pb_2Ru_2O_{6.5}$) as an efficient bifunctional oxygen electrocatalyst. In the sol-gel process (Fig. 16b), the A- and B-site cations were crosslinked using citric acid as the chelating agent. Then, the pyrochlore oxides were crystallized using a heat treatment method at 650 °C for $Pb_2Ru_2O_{6.5}$ and

1050 °C for $Sm_2Ru_2O_7$. $Pb_2Ru_2O_{6.5}$ exhibited outstanding bifunctional catalytic activities and stabilities for ORR and OER in aqueous ZABs.

Senthilkumar et al. [21] synthesized bifunctional noble metal-free $Co_3(PO_4)_2$ nanostructures through the facile precipitation technique and evaluated their electrocatalytic activities. $Co(NO_3)_2 \cdot 6H_2O$ and $NH_4H_2PO_4$ were dissolved in distilled H_2O. NaOH aqueous solution (1 M) was added, and the pH was adjusted to 7. After 5 h of stirring, the precipitate was collected and dried at 80 °C overnight. After calcination at 700 °C for 5 h, the pure phase of $Co_3(PO_4)_2$ was obtained. As an electrocatalyst, $Co_3(PO_4)_2$ delivered low overpotential of 0.59 V, and its round trip energy efficiency reached 83%. The SAB exhibited stable cycle performance of up to 50 cycles. Chen et al. [210] reported an easy and effective soft-template method to in-situ encode Fe_2N NPs on the surface of N-doped graphene-like carbon (NC; Fig. 16c). The prepared Fe_2N NPs were covered with a few carbon layers, which promoted the connection of Fe–NX clusters with graphene to facilitate the formation of Fe–N–C active sites. The Fe–NX and NC units enabled different catalytic functionalities and resulted in excellent catalytic performance.

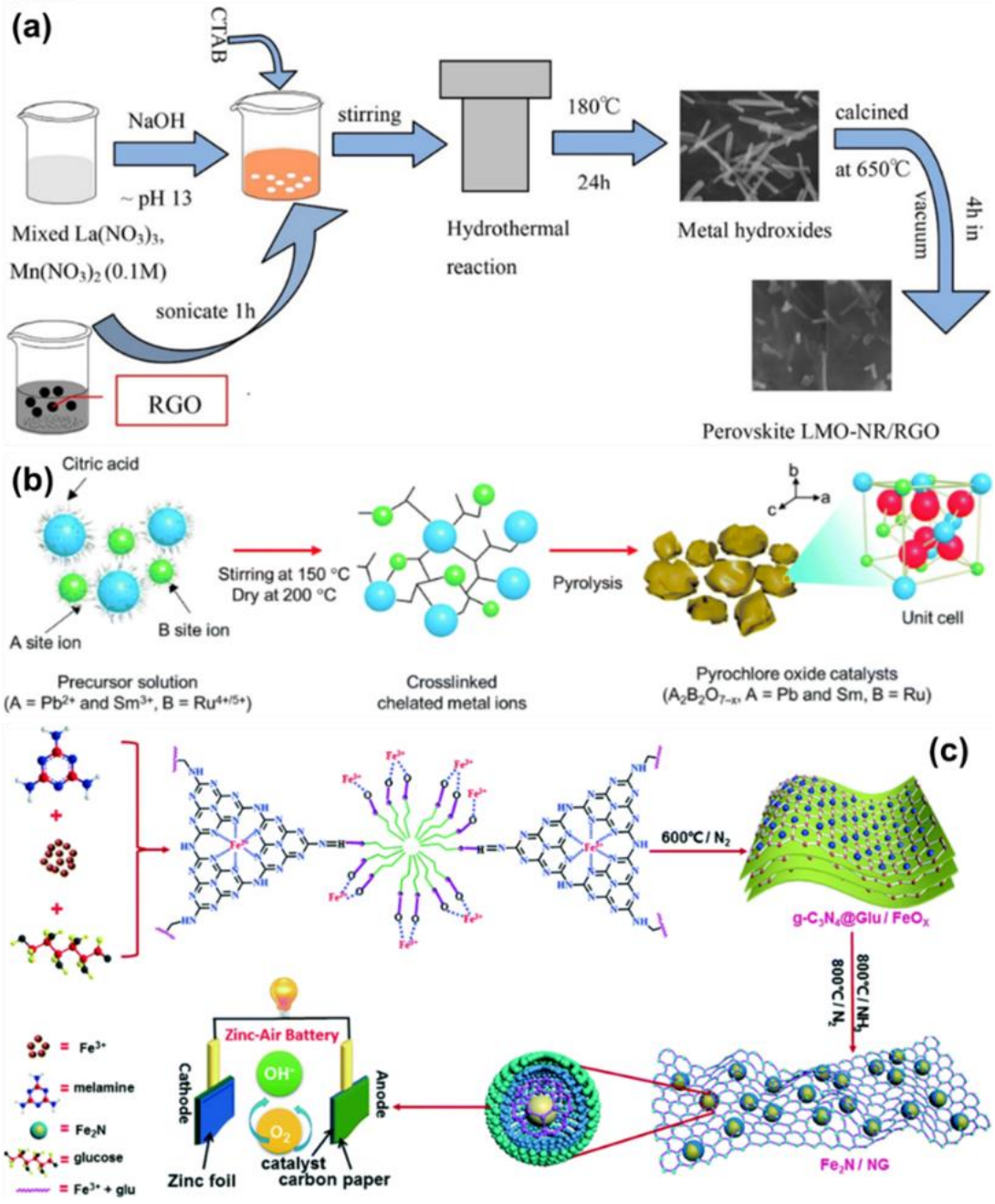

Fig. 16 (a) Schematic of the hydrothermal synthesis of LMO-NR/RGO [208]. Copyright 2017, Elsevier. (b) Preparation and characterization of the morphologies and structures of highly pure single crystalline pyrochlore oxide NPs ($A_2B_2O_{7-x}$, A = Pb and Sm, B = Ru). Schematic of the preparation of highly pure single crystalline pyrochlore oxide NPs. During the sol-gel process, A-site cations (blue spheres) are crosslinked with B-site cations (green spheres) by citric acid (black lines). After heat treatment at

different temperatures (650 °C for $Pb_2Ru_2O_{6.5}$ and 1050 °C for $Sm_2Ru_2O_7$), the powdered pyrochlore members (red-brown solid figures) are synthesized [209]. Copyright 2017, Royal Society of Chemistry. (c) Schematic of the preparation and features of Fe_2N@NC [210]. Copyright 2017, Royal Society of Chemistry.

3.2.2. Electrospinning

Compared with traditional wet-chemistry methods, electrospinning is a simple and effective technology that offers greater advantages in the design of materials structure and morphology without using any template [211, 212], having applications in biomedical materials, filtration and protection, catalysis, energy, food engineering, cosmetics and polymer electrolyte membrane in fuel cell [213-215]. Generally, the structures and morphologies of products are highly dependent on the molecular weights of the polymer, solution properties (concentration, viscosity, conductivity, surface tension, and liquid flow), electromotive force, distance between capillary and collection screen, and environmental parameters (temperature, humidity, and indoor air flow rate) [216–218]. Liu et al. [219] prepared 1D $FeVO_4$ nanobelts with a width of about 400 nm through a simple electrospinning process followed by calcination. Wang et al. [220] synthesized a branch-like hierarchical γ-Bi_2MoO_6 nanostructure and 1D $Bi_2Mo_xW_{1-x}O_6$ (x = 0, 0.2, 0.5, 0.67, and 1) [221] by combining electrospinning and sintering techniques. Cao et al. [222] prepared a 3D hierarchical porous CNFs with different loading amounts of Co through electrospinning combined with a thermal annealing process. Wang et al. [223] designed a novel nanofibrous bifunctional electrocatalyst

film, consisting of metallic manganese sulfide and Co encapsulated by N-doped CNFs (CMS/NCNFs), using a continuous electrospinning method followed by carbonization. The CMS/NCNF bifunctional catalyst exhibited ORR and OER performance that is comparable to those of commercial precious metal-based catalysts.

Especially in the design of one-dimensional nanomaterials, electrospinning technology has more obvious advantages. Zhang et al. [224] prepared porous ultra long $La_{0.6}Sr_{0.4}Co_{0.8}Mn_{0.2}O_3$ nanofibers (LSCM NFs) through electrospinning (Fig. 17a). RuO_2 NPs were deposited on the surface of LSCM NFs by chemical impregnation. The Li-O_2 cell with RuO_2@LSCM NF catalyst exhibited high specific discharge capacity (12741.7 mAh g^{-1}), improved cyclability and rate capability, and low voltage gap (0.79 V at 10 mA cm^{-2}). Wang et al. [225] produced a mesoporous N-doped thin-walled $CuCo_2O_4$@C nanotubes by electrospinning technique. As a bifunctional oxygen electrocatalyst for ZABs, the as-prepared $CuCo_2O_4$@C with a specific surface area of 514 m^2 g^{-1} exhibited a positive half-wave potential of 0.85 V for the ORR and a low overpotential of 327 mV at 10 mA cm^{-2} for the OER (Fig. 17b, c). Zhao et al. [226] developed an in-situ growth method to produce 1D structure-controllable zeolitic imidazolate frameworks (ZIFs)/polyacrylonitrile (PAN) core/shell fiber (PAN@ZIFs) through electrospinning. The fiber diameter (after pyrolysis) was 500 nm, with <20 nm metal particles existed in the interior of the optimized catalyst (Figs. 17d and 17e), which exhibited prominent bifunctional ORR/OER catalytic activity and durability. Through electrospinning, Alegre et al. [227] synthesized CNFs with cobalt oxide and Co (CoO-Co/CNFs) as bifunctional air electrodes for metal-air batteries. These CoO-

Co/CNFs exhibited polarization at high electrochemical potentials (2 V vs RHE), rapid charge-discharge cycles at ±80 mA cm^{-2}, and long durability through charging for 12 h at 60 mA cm^{-2} and discharging for 8 h at −80 mA cm^{-2} (Fig. 17f).

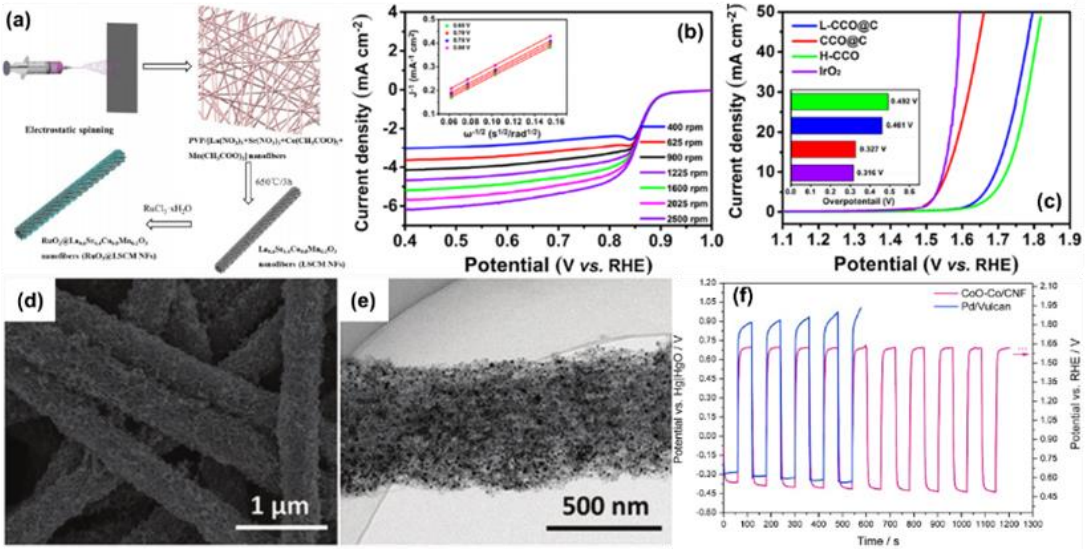

Fig. 17 (a) Schematic of the synthesis of LSCM NFs and RuO_2@LSCM NFs [224]. Copyright 2017, American Chemical Society. (b) ORR polarization curves of the CCO@C nanotubes at different rotation speeds and the corresponding K−L plots at different potentials (inset). (c) OER polarization curves of L-CCO@C, CCO@C, H-CCO, IrO_2, and the overpotential schematic at 10 mA cm^{-2} (inset) [225]. Copyright 2017, American Chemical Society. (d) SEM and (e) TEM images of CNF@Zn/CoNC [226]. Copyright 2018, Elsevier. (f) Charge/discharge cycles at ± 80 mA cm^{-2} of the assessed catalysts [227]. Copyright 2017, Elsevier.

3.2.3. Atomic Layer Deposition

Atomic layer deposition (ALD) is an advanced deposition technique for preparing ultrathin films and low-dimensional nanomaterials, which employs self-limiting

chemical reactions to control film thickness and composition [228]. Uniform, conformal and permeable coatings can be formed on the surfaces with complex topographies [229]. ALD is ideal for designing highly efficient and durable catalysts for batteries [230]. Numerous metal oxides, such as Al_2O_3, ZnO, ZrO_2, TiO_2, and Fe_2O_3, have been researched using ALD [231, 232]. Lei et al. [233] first demonstrated the ALD of Pd NPs on a porous carbon support as a catalyst for LABs. Xie et al. [234] reported the ALD of Ru NPs on the 3D nanostructured $TiSi_2$ substrate as a high-performance catalyst for LABs. Schroeder et al. [235] reported the ALD of RuO_2 on multiwalled CNT sponge substrates as long life air electrodes for LABs. Cheng et al. [236, 237] reported the ALD of stabilized Pt/ZrC and Pt/ZrO_2 electrocatalysts for ORR in fuel cells. They also reported a novel hierarchical nanostructured Co_3O_4 decorated on CNTs by ALD (CNT@Co_3O_4) and used it as a catalyst for SABs [115]. Well-dispersed ALD of Co_3O_4 on CNTs served as functionalized active sites and enabled rapid electron exchange and high oxygen reduction/evolution activities

Different types of catalysts can be designed by ALD technology, including oxides, carbon materials, perovskite, and their composites. Gong et al. [166] proposed an integrated ALD iron oxide and perovskite $LaNiO_3$ as a novel catalyst for OER and ORR. Fig. 18a illustrates the fabrication of the integrated $LaNiO_3$-Fe_2O_3 core/shell structure. The $LaNiO_3$ particles aggregated and formed a continuous 2D network structure via the ALD preparation. The synthesized 2D network is highly suitable for electrode structure in Li-O_2 batteries because the interconnected channels can benefit electronic and ionic transportation. Lu et al. [238] prepared a cathode that utilized the ALD of Pd NPs on a

carbon surface with an alumina coating for the passivation of carbon defect sites (Fig. 18b), achieving a low charge overpotential of 0.02 V. Li et al. [239] synthesized a novel and efficient bifunctional OER/ORR catalyst of Co_9S_8/CNT through ALD (Figs. 18c and 18d). TEM results revealed that a uniform 7 nm Co_9S_8 layer was conformally coated on the entire CNT, demonstrating that the ALD coating layer was highly uniform and conformal (Figs. 18e and 18f).

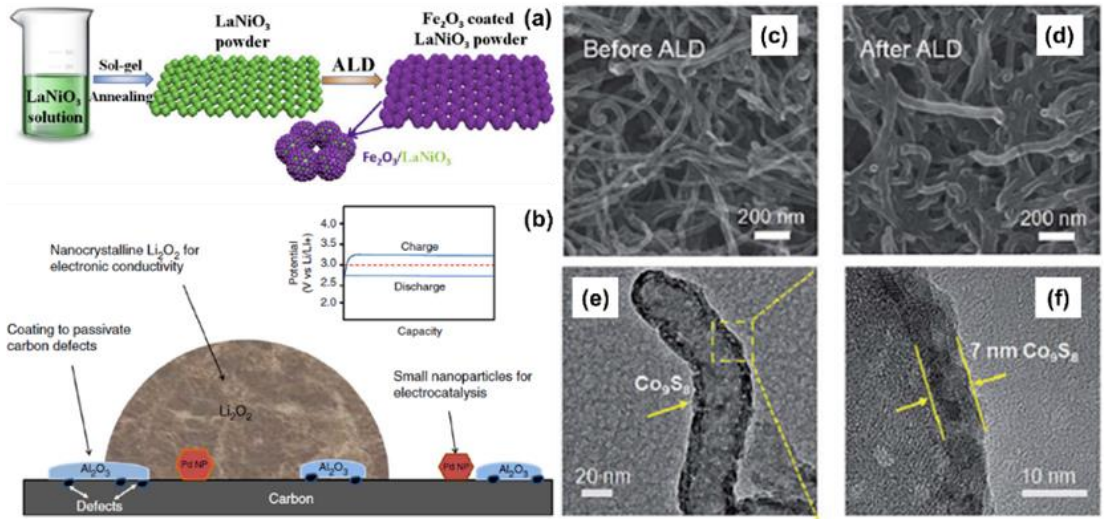

Fig. 18 (a) Fabrication schematics of integrated ALD-Fe_2O_3/$LaNiO_3$ catalyst with core/shell structure [166]. Copyright 2018, Elsevier. (b) Al_2O_3 coating, palladium NPs, and nanocrystalline lithium peroxide decrease overpotential. Inset shows a hypothetical charge/discharge voltage profile versus capacity [238]. Copyright 2014, Springer. SEM images of (c) uncoated CNTs and (d) ALD Co_9S_8/CNT. (e and f) TEM images of an ALD Co_9S_8-coated CNT [239]. Copyright 2017, Royal Society of Chemistry.

Various synthesis approaches can be selected according to the requirements of the catalysts for HSABs. The following principles can be applied in the selection: (1) the

hydrothermal approach provides an ease of controlling of the morphology; (2) the sol-gel approach offers homogeneous uniform at molecular-level for powder catalysts; (3) the precipitation approach is simple and mass-scalable; and (4) the template, electrospinning, and ALD approaches enable the design of advanced structures. In electrospinning, the structures and morphologies of the products can be optimized by adjusting polymer molecular weight, solution properties, electromotive force, the distance between capillary and collection screen, and environmental parameters. Meanwhile, ALD approach not only enables highly uniform and conformal coatings on the surfaces of conductive current collectors with complex topographies, but also allows infiltration on mesoporous materials. The structure and dimension control of bifunctional catalysts by electrospinning and ALD technology will be an important way to improve their activity and utilization. It is anticipated that ALD technique is ideal for designing highly efficient and durable catalysts for metal-air batteries. The future development of next-generation high-performance HSABs could be realized by combining various synthesis methods for obtaining catalysts with superior structural and electrocatalytic properties.

4. Perspectives on HSABs

4.1. Anode

In HSABs, Na metal anode plays a critical role in the performance and safety issue of the batteries. Studies have shown that Na dendrite growth is the key factor to affect the lifetime of HSABs. Moreover, the dissolution and the precipitation rates of Na metal

during fast charging and discharging processes directly affect the performance of HSABs. Therefore, protection of Na metal by traditional methods such as surface treatment of Na anode and electrolyte modification for high-rate performance HSABs will be an important research direction. Our study in suppression of dendritic lithium formation in Li-ion battery suggested that construction of porosity in metallic anode may be an effective method for increasing its specific surface area, which may accelerate the dissolution and the precipitation of metallic anode in electrochemical processes, leading to inhabitation of the growth of the dendrites [240]. Very recently, our study [22] have proved that liquid-Na anode can effectively improve the high-rate performance and the reversibility of HSABs. These studies may provide new insights into tackling the growth of Na dendrite at the high-rate performance of HSABs.

4.2. Electrolyte

The electrolyte in HSABs is divided into the aqueous electrolyte and aprotic electrolyte. The aqueous electrolyte is NaOH solution and its concentration is mostly 0.1 M or 1 M. How the higher concentration of aqueous electrolyte affects the charge-discharge voltage profile of HSABs, that has not been clearly investigated. As the selection of aprotic electrolyte in HSABs has been followed from the traditional SABs, the development of a new electrolyte system is necessary. In particular, the influence of various electrolyte additives on battery charge-discharge voltage profile, battery polarization, the formation of good SEI film and battery stability are critical areas for future research on high-performance HSABs.

4.3. Air electrode

The greatest advantage of metal-air batteries is their intrinsic high energy density because oxygen is free from the air. Besides the dissolution and the deposition of metals on the anode, effective operation of metal-air batteries relies on the reactions of oxygen reduction and oxygen evolution on air electrode. The compositions and the structural stability of catalysts are the key factors affecting the HSABs' performance. However, related research is rarely studied so far. More studies on the compositions and structure of the catalysts after battery cycling test or conducting in-situ analysis the compositions and structure of catalysts during the charge-discharge processes are necessary for the future research of HSABs, which provide theoretical guidance for improving the cycle stability of catalysts.

Similar to ZABs, alkaline water electrolyzer, and fuel cells, the performance of HSABs relies on highly efficient air electrodes. In general, air electrodes of metal-air batteries should possess low overpotential, high bifunctional catalytic activities, high stability, high CO_2 tolerance, and good water management ability [241, 242]. Although HSAB research is still in its infancy, the development of highly efficient air electrode is expected to play a critical role in the future development of high-performance HSABs (Fig. 19).

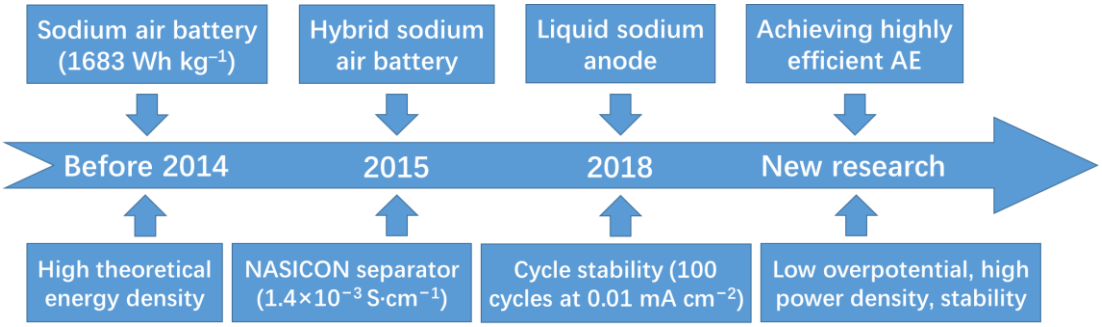

Fig. 19 Research progress and development trend of HSABs.

There are four key areas for achieving a highly efficient air electrode for HSABs. Firstly, the catalytic activity of electrocatalysts directly affects the power density of HSABs [243, 244], In catalyst design for air electrodes (Section 3), we reviewed the classification of electrocatalysts based on some metal-air batteries. MOFs have high catalytic potential because of their high specific surface area and tunable porous structure. Different MOFs derivatives can be obtained by adjusting the heat treatment process. A careful design of SAC-carbon composites using MOFs as precursors can provide anticipated highly efficient electrocatalysts for HSABs. Moreover, using electrospinning and ALD technology to design the structure and the morphology of the air electrode will be conducive to the realization of the expected performance of the catalyst. Secondly, the stability of electrocatalysts is vital to the cycle life of HSABs. Although catalysts do not participate in the formation of reaction products in the catalytic process, the compositions and the structure of electrocatalysts may be destroyed due to the erosion of alkaline electrolyte and the impact of charge-discharge current. To improve the cycle life of metal-air batteries, the evolution of the catalyst's stability needs to be investigated. Thirdly, CO_2 poisoning may be one of the potential

influencing factors affecting the cycle performance of HSABs. Previous researches on alkaline water electrolyzer and fuel cells have proved that an effective way to solve this problem is to design and synthesize CO_2 tolerant catalysts with abundant active sites [104]. Fourthly, the architectural design of air electrode with a good interface is a key to control water management. In addition, it is necessary to study the failure mechanism of the air electrode during charge-discharge cycles.

As an important component of HSABs, the architectural design of the air electrode is very important. To avoid the battery failure caused by the volatilization of aqueous electrolyte in HSABs, a sandwich structure of the air electrode can be utilized, consisting of a waterproof gas permeable layer, a current collector and a catalytic layer. The fuel cell research has proved that it is a good choice to prepare the waterproof gas permeable layer and the catalytic layer by using PTFE and Nafion [111, 112]. However, the current collector should be further designed to achieve higher infiltration and flexibility for adhering the waterproof gas permeable layer and the catalytic layer. Moreover, the amount of PTFE and Nafion in the catalytic layer needs to be optimized to prevent the occlusion of the catalytic active sites in the catalytic layer.

5. Conclusions and outlook

Global energy crisis and environmental pollution from fossil fuels have aroused widespread concern in the development of high-performance energy storage systems that can integrate with intermittent renewable energy sources. HSABs have received considerable attention owing to their high theoretical specific energy, high sodium

abundance, low-cost, and environment-friendliness. Compared with SABs, HASBs have a simple reaction process, aqueous discharge product, and high theoretical operation voltage. These merits pave the way for next-generation high-performance energy storage systems. Electrocatalysts with distinct characteristics can be synthesized by various synthesis approaches, providing a rich selection for the design of air electrodes for HSABs.

Many HSABs have been studied at the laboratory level by using coin cells, and their electrochemical performance has continuously improved. Nevertheless, studies in this field are at an early stage. Many challenges in the components of HSABs need to be addressed before practical industrial applications become possible. First, producing large-scale cells with good current discharge performance and cycle stability remains challenging. A complete cell encapsulation with aqueous and aprotic electrolytes can reduce the overpotential and improve cycle life. However, the use of NASICON separator may be the bottleneck to the large-scale manufacturing of HSABs. In addition, various energy and electronic devices have been made flexible for military and other special applications. Flexible sodium-ion conductor materials need to be developed. Second, dendrites formation on Na anode surface during the electrochemical cycle pose safety hazards and accelerate the deterioration of battery performance. The design of self-healing of Na dendrite anode structure is an urgent issue. Third, the selection of aprotic electrolyte is another issue that need to be addressed. The types of aprotic electrolytes are highly diverse. The electrolyte considerably affects the operating voltage of a battery and the formation of SEI films on Na anode surfaces. The

electrolyte type, modification, and additive addition can directly affect battery performance. Finally, the design of air electrodes, especially the synthesis and optimization of electrocatalysts, have a significant impact on the development of high-performance HSABs. Among various electrocatalysts, SACs/carbon composites are potential bifunctional electrocatalysts in metal-air batteries because they exhibit high efficiency in ORR and OER. Adjusting the structure and morphology of the electrocatalyst by utilizing special techniques, such as electrospinning and ALD, are effective approaches for improving HSAB performance.

In summary, HSABs are promising high-energy and high-power energy storage devices. As an emerging battery technology, HSABs production presents enormous opportunities, as well as challenges. Extra efforts are necessary for the (1) development of simple yet efficient methods for the synthesis and the modification of the electrocatalysts in air electrode with excellent electrochemical performance; (2) exploration of other types of Na ion conductor separator for the production of large-scale HSABs; and (3) development of effective approaches to suppress Na dendrite growth. HSABs are expected to be developed as competitive technologies for energy storage and as a solution for various energy-related challenges. Nevertheless, future development in HSABs should be enthralling.

Acknowledgment: This work was supported by the Doctoral Innovation Scholarship of Beijing University of Technology, the Scholarship from China Scholarship Council of China (CSC NO. 201806540025), the Science and Technology Development Fund

of the Macau SAR (FDCT098/2015/A3 and FDCT191/2017/A3), the Multi-Year Research Grants (MYRG2017-00216-FST and MYRG2018-00192-IAPME) from the Research Services and Knowledge Transfer Office at the University of Macau, and the UEA funding.

References

[1] T. Ling, D. Yan, Y. Jiao, H. Wang, Y. Zheng, X. Zheng, J. Mao, X. Du, Z. Hu, M. Jaroniec, S. Qiao, *Nat. Commun.* **2016**, 7, 12876.

[2] J. R. Han, S. Hao, Z. A. Liu, A. M. Asiri, X. P. Sun, Y. H. Xu, *Chem. Commun*. **2018**, 54, 1077.

[3] X. L, Xu, C. Y. Qi, Z. D. Hao, H. Wang, J. T. Jiu, J. B. Liu, H. Yan, K. Suganuma, *Nano-Micro Lett.* **2018**, 10, 1.

[4] X. L. Xu, Z. D. Hao, H. Wang, C. Hu, J. B. Liu, Y. Jin, *Ionics* **2018**, 25, 89.

[5] K. X. Lei, C. C. Wang, L. J. Liu, Y. W. Luo, C. N. Mu, F. J. Li, J. Chen, *Angew. Chem.* **2018**, 130, 4777.

[6] I. W. Ock, J. W. Choi, H. M. Jeong, J. K. Kang, *Adv. Energy Mater.* **2018**, 8, 1702895.

[7] Z. Zhang, L. L. Kong, S. Liu, G. R. Li, X. P. Gao, *Adv. Energy Mater.* **2017**, 7, 1602543.

[8] X. Fang, H. Peng, *Small* **2015**, 11, 1488.

[9] A. Manthiram, Y. Z. Fu, S. H. Chung, C. X. Zu, Y. S. Su, *Chem. Rev.* **2014**, 114, 11751.

[10] J. Pan, H. P. Li, H. Sun, Y. Zhang, L. Wang, M. Liao, X. M. Sun, H. S. Peng, *Small* **2018**, 14, 1703454.

[11] Z. Khan, B. Senthilkumar, S. O. Park, S. Park, J. C. Yang, J. H. Lee, H. K. Song, Y. Kim, S. K. Kwak, H. Ko, *J. Mater. Chem. A* **2017**, 5, 2037.

[12] P. Moni, S. Hyun, A. Vignesh, S. Shanmugam, *Chem. Commun.* **2017**, 53, 7836.

[13] Y. F. Xu, Y. Zhao, J. Ren, Y. Zhang, H. S. Peng, *Angew. Chem.* **2016**, 128, 8111.

[14] J. Fu, D. U. Lee, F. M. Hassan, L. Yang, Z. Y. Bai, M. G. Park, Z. W. Chen, *Adv. Mater.* **2015**, 27, 5167.

[15] M. Prabu, P. Ramakrishnan, P. Ganesan, A. Manthiram, S. Shanmugam, *Nano Energy* **2015**, 15, 92.

[16] S. K. Das, S. Lau, L. A. Archer, *J. Mater. Chem. A*, **2014**, 2, 12623.

[17] S. Ha , J. K. Kim , A. Choi, Y. Kim, K. T. Lee, *ChemPhysChem* **2014**, 15, 1971.

[18] X. L. Xu, S. J. Wang, H. Wang, C. Hu, Y. Jin, J. B. Liu, H. Yan, *J. Energy Chem.* **2018**, 27, 513.

[19] S. H. Sahgong, S. T. Senthilkumar, K. Kim, S. M. Hwang,Y. Kim, *Electrochem. Commun.* **2015**, 61, 53.

[20] K. Hayashi, K. Shima, F. Sugiyama, *J. Electrochem. Soc.* **2013**, 160, A1467.

[21] B. Senthilkumar, Z. Khan, S. Park, I. Seo, H. Ko, Y. Kim, *J. Power Sources* **2016**, 311, 29.

[22] F. Liang, X. C. Qiu, Q. K. Zhang, Y. Kang, A. Koo, K, Hayashi, K. F. Chen, D. F. Xue, K. N. Hui, H. Yadegari, X. L. Sun, *Nano Energy* **2018**, 49, 574.

[23] K. Song, D. A. Agyeman, M. Park, J. Yang, Y. M. Kang, *Adv. Mater.* **2017**, 29, 1606572.

[24] B. Sun, K. Kretschmer, X. Xie, P. Munroe, Z. Peng, G. Wang, *Adv. Mater.* **2017**, 29, 1606816.

[25] Y. Zhao, L.V. Goncharova, Q. Zhang, P. Kaghazchi, Q. Sun, A. Lushington, B. Wang, R. Li, X. Sun, *Nano Lett.* **2017**, 17, 5653.

[26] J. Yu, Y. S. Hu, F. Pan, Z. Zhang, Q. Wang, H. Li, X. Huang, L. Chen, *Nat. Commun.*

2017, 8, 14629.

[27] Z. Khan, S. Park, S. M. Hwang, J. Yang, Y. Lee, H. K. Song, Y. Kim, H. Ko, *NPG Asia Mater.* **2016**, 8, e294.

[28] L. Li, X. Zhao, A. Manthiram, *Electrochem. Commun.* **2012**, 14, 78.

[29] P. Bilski, B. Marczewska, *Nuclear Instruments and Methods in Physics Research Section B: Beam Interactions with Materials and Atoms* **2017**, 392, 41.

[30] T. Rojo, Y. S. Hu, M. Forsyth, X. L. Li, *Adv. Energy Mater.* **2018**, 8, 1800880.

[31] W. M. Haynes, CRC handbook of chemistry and physics. CRC press, 2014.

[32] N. Parveen, S. A. Ansari, H. R. Alamri, M. O. Ansari, Z. Khan, M. H. Cho, *Electrochim. Acta* **2017**, 257, 328.

[33] E. F. Simon, A. Natan, E. Peled, D. Golodnitsky, *J Solid. State Electrochem.* **2018**, 22, 1015.

[34] T. Hashimoto, K. Hayashi, *Electrochim. Acta,* **2015**, 182, 809.

[35] Z. E. M. Reeve, C. J. Franko, K. J. Harris, H. Yadegari, X. L. Sun, G. R. Goward, *J. Am. Chem. Soc.* **2017**, 139, 595.

[36] L. Schafzahl, N. Mahne, B. Schafzahl, M. Wilkening, C. Slugovc, S. M. Borisov, S. A. Freunberger, *Angew. Chem. Int. Edit.* **2017**, 56, 15728.

[37] Y. Zheng, Y. Jiao, Y. H. Zhu, Q. R. Cai, A. Vasileff, L. H. Li, Y. Han, Y. Chen, S. Z. Qiao, *J. Am. Chem. Soc.* **2017**, 139, 3336.

[38] B. E. Conway, T. C. Liu, *Langmuir* **1990**, 6, 268.

[39] V. I. Birss, A. Damjanovic, P. G. Hudson, *J. Electrochem. Soc.* **1986**, 133, 1621.

[40] S. Ressel, F. Bill, L. Holtz, N. Janshen, A. Chica, T. Flower, C. Weidlich, T.

Struckmann, *J. Power Sources*, **2018**, 378, 776.

[41] M. Zhou, Q. H. Weng, X. Y. Zhang, X. Wang, Y. M. Xue, X. H. Zeng, Y. Bando, D. Golberg, *J. Mater. Chem. A*, **2017**, 5, 4335.

[42] W. Li, N. Jiang, B. Hu, X. Liu, F. Z. Song, G. Q. Han, T. J. Jordan, T. B. Hanson, T. L. Liu, Y. J. Sun, *Chem.* **2018**, 4, 637.

[43] W. R. Cheng, X. Zhao, H. Su, F. M. Tang, W. Che, H. Zhang, Q. H. Liu, *Nat. Energy* **2019**, 4, 115.

[44] O. T. Holton, J. W. Stevenson, *Platin. Met. Rev.* **2013**, 57, 259.

[45] R. F. de Morais, A. A. Franco, P. Sautet, D. Loffreda, *Phys. Chem. Chem. Phys.* **2015**, 17, 11392.

[46] C. C. L.McCrory, S. Jung, J. C. Peters, T. F. Jaramillo, *J. Am. Chem. Soc.* **2013**, 135, 16977.

[47] Y. Kang, F. Liang, K. Hayashi, *Electrochim. Acta*, **2016**, 218, 119.

[48] M. Kim, H. Ju, J. Kim, *J. Mate. Chem. A* **2018**, 6, 8523.

[49] M. Kim, H. Ju, J. Kim, *Dalton Trans.* **2018**, 47, 15217.

[50] M. Kim, H. Ju, J. Kim, *Chem. Engin. J.* **2019**, 358, 11.

[51] Y. I. Wu, X. C. Qiu, F. Liang, Q. K. Zhang, A. Koo, Y. N. Dai, Y. Lei, X. L. Sun, *Appl. Catal. B-Environ.* **2019**, 241, 407.

[52] J. Y. Cheon, K. Kim, Y. J. Sa, S. H. Sahgong, Y. Hong, J. Woo, S. D. Yim, H. Y. Jeong, Y. Kim, S. H. Joo, *Adv. Energy Mater.* **2016**, 6, 1501794.

[53] F. Liang, T. Watanabed, K. Hayashie, Y. C. Yao, W. H. Ma, B. Yang, Y. N. Dai, *Mater. Lett.* **2017**, 187, 32.

[54] S. M. Hwang, W. Go, H. Yu, Y. Kim, *J. Mater. Chem. A* **2017**, 5, 11592.

[55] Y. Kang, F. M. Su, Q. K. Zhang, F. Liang, K. R. Adair, K. F. Chen, D. F. Xue, K. Hayashi, S. C. Cao, H. Yadegari, X. L. Sun, *ACS Appl. Mater. Interfaces* **2018**, 10, 23748.

[56] M. Abirami, S. M. Hwang, J. C. Yang, S. T. Senthilkumar, J. Kim, W. S. Go, B. Senthilkumar, H. K. Song, Y. Kim, *ACS Appl. Mater. Interfaces* **2016**, 8, 32778.

[57] Z. Khan, N. Parveen, S. A. Ansari, S. T. Senthilkumar, S. Park, Y. Kim, M. H. Cho, H. Ko, *Electrochim. Acta*, **2017**, 257, 328.

[58] W. W. Yin, Z. W. Fu, *ChemCatChem*, **2017**, 9, 1545.

[59] Y. Liu, P. He, H. Zhou, *Adv. Energy Mater.* **2018**, 8, 1701602.

[60] J. Pan, Y. Y. Xu, H. Yang, Z. H. Dong, H. F. Liu, B. Y. Xia, *Adv. Sci.* **2018**, 5, 1700691.

[61] W. M. Liu, W. W. Yin, F. Ding, L. Sang, Z. W. Fu, *Electrochem. Commun.* **2014**, 45, 87.

[62] K. B. Hueso, V. Palomares, M. Armand, T. Rojo, *Nano Res.* **2017**, 10, 4082.

[63] X. L. Xu, S. J. Wang, H. Wang, B. Xu, C. Hu, Y. Jin, J. B. Liu, H.Yan, *J. Energy Storage*, **2017**, 13, 387.

[64] F. Aguesse, W. Manalastas, L. Buannic, J. M. L. del Amo, G. Singh, A. Llordés, J. Kilner, *ACS Appl. Mater. Interfaces* **2017**, 9, 3808.

[65] R. Zhang, X. B. Cheng, C. Z. Zhao, H. J. Peng, J. L. Shi, J. Q. Huang, J. F. Wang, F. Wei, Q. Zhang, *Adv. Mater.* **2016**, 28, 2155.

[66] F. Ding, W. Xu, G. L. Graff, J. Zhang, M. L. Sushko, X. L. Chen, Y. Y. Shao, M.

H. Engelhard, Z. Nie, J. Xiao, X. J. Liu, P. V. Sushko, J. Liu, J. G. Zhang, *J. Am. Chem. Soc.*, **2013**, 135, 4450.

[67] P. Hartmann, C. L. Bender, J. Sann, A. K. Durr, M. Jansen, J. J. P. Adelhelm, *Phys. Chem. Chem. Phys.* **2013**, 15, 11661.

[68] Y. S. Hong, N. Li, H. Chen, P. Wang, W. L. Song, D. N. Fang, *Energy Storage Mater.* **2018**, 11, 118.

[69] J. Sun, H. W. Lee, M. Pasta, H. T. Yuan, G. Y. Zheng, Y. M. Sun, Y. Z. Li, Y. Cui, *Nat. Nanotechn.* **2015**, 10, 980.

[70] X. Zhang, X. G. Wang, Z. J. Xie, Z. Zhou, *Green Energy & Environment* **2016**, 1, 4.

[71] J. M. Zheng, J. A. Lochala, A. Kwok, Z. D. Deng, J. Xiao, *Adv. Sci.* **2017**, 4, 1700032.

[72] S. C. Wu, Y. Qiao, K. Z. Jiang, Y. B. He, S. H. Guo, H. S. Zhou, *Adv. Funct. Mater.* **2018**, 28, 1706374.

[73] P. Kubisiak, A. Eilmes, *J. Phys. Chem. B* **2017**, 121, 9957.

[74] J. H. Song, B. W. Xiao, Y. H. Lin, K. Xu, X. L. Li, *Adv. Energy Mater.* **2018**, 8, 1703082.

[75] H. W. Zhang, X. D. Huang, O. Noonan, L. Zhou, C. Z. Yu, *Adv. Funct. Mater.* **2017**, 27, 1606023.

[76] L. Lutz, D. A. D. Corte, M. X. Tang, E. Salager, M. Deschamps, A. Grimaud, L. Johnson, P. G. Bruce, J. M. Tarascon, *Chem. Mater.* **2017**, 29, 6066.

[77] J. Wang, S. Y. Che, Z. W. Zhao, S. Ashraf, D. Wexlerc, J. Chen, S. H. Ng, S. L.

Chou, H. K. Liu, *Carbon* **2008**, 46, 229.

[78] X. G. Sun, X. Wang, R. T. Mayes, S. Dai, *ChemSusChem* **2012**, 5, 2079.

[79] Y. Yan, Y. X. Yin, S. Xin, J. Su, Y. G. Guo, L. J. Wan, *Electrochim. Acta* **2013**, 91, 58.

[80] G. Q. Ma, Z. Y. Wen, J. Jin, M. F. Wu, G. X. Zhang, X. W. Wu, J. C. Zhang, *Solid State Ionics* **2014**, 262, 174.

[81] J. S. Kim, T. H. Hwang, B. G. Kim, J. Min, J. W. Choi, *Adv. Funct. Mater.* **2014**, 24, 5359.

[82] X. S. Huang, *J. Solid State Electrochem.* **2011**, 15, 649.

[83] P. Arora, Z. Zhang, *Chem. Rev.* **2004**, 35, 4419.

[84] S. S. Zhang, *J. Power Sources* **2007**, 164, 351.

[85] J. Duay, M. Kelly, T. N. Lambert, *J. Power Sources*, **2018**, 395, 430.

[86] J. B. Goodenough, H. Y. Hong, J. A. Kafalas, *Mater. Res. Bull.* **1976**, 11, 203.

[87] R. O. Fuentes, F. M. Figueiredo, F. M. B. Marques, J. I. Franco, *Solid State Ionics* **2001**, 140, 173.

[88] R. O. Fuentes, F. M. Figueiredo, F. M. B. Marques, J. I. Franco, *J. Eur. Ceram. Soc.* **2001**, 21, 737.

[89] K. Noi, K. Suzuki, N. Tanibata, A. Hayashi, M. Tatsumisago, *J. Am. Ceram. Soc.* **2018**, 101, 1255.

[90] F. Liang, K. Hayashi, *J. Electrochem. Soc.* **2015**, 162, A1215.

[91] Y. H. Cheng, G. Chen, H. B. Wu, M. F. Zhu, Y. F. Lu, *J. Mater. Chem. A* **2017**, 5, 13944.

[92] J. W. Zhao, K. K. Sonigara, J. J. Li, J, Zhang, B. B. Chen, J. J. Zhang, S. S. Soni, X. H. Zhou, G. L. Cui, L. Q. Chen, *Angew. Chem.* **2017**, 129, 7979.

[93] X. F. Ding, Z. P. Gao, D. Ding, X. Y. Zhao, H. Y. Hou, S. H. Zhang, G. L. Yuan, *Appl. Catal. B-Environ.* **2019**, 243, 546.

[94] Y. Yin, J. Liu, Y. F. Chang, Y. Z. Zhu, X. Xie, Y. Z. Qin, J. F. Zhang, K. Jiao, Q. Du, M. D. Guiver, *Electrochim. Acta* **2019**, 296, 450.

[95] Z. Q. Wang, L. J. Qu, Y. C. Zeng, X. Q. Guo, Z. G. Shao, B. L. Yia, *RSC Adv.* **2018**, 8, 1503.

[96] A. G. Divekar, B. S. Pivovar, A. M. Herring, *ECS Trans.* **2018**, 86, 643.

[97] P. Qiu, A. Wang, H. Y. Zheng, L. C. Jia, B. Chi, J. Pu, J. Li, *Intern. J. Hydrogen Energy* **2018**, 43, 20696.

[98] H. Yadegari, Q. Sun, X. L. Sun, *Adv. Mater.* **2016**, 28, 7065.

[99] S. A. Freunberger, Y. H. Chen, Z. Q. Peng, J. M. Griffin, L. J. Hardwick, F. Barde, P. Novak, P. G. Bruce, *J. Am. Chem. Soc.* **2011**, 133, 8040.

[100] B. D. McCloskey, A. Speidel, R. Scheffler, D. C. Miller, V. Viswanathan, J. S. Hummelshoj, J. K. Norskov, A. C. Luntz, *J. Phys. Chem. Lett.* **2012**, 3, 997.

[101] Y. S. Mekonnen, K. B. Knudsen, J. S. G. Mýrdal, R. Younesi, J. Højberg, J. Hjelm, P. Norby, T. Vegge, *J. Chem. Phys.* **2014**, 140, 121101.

[102] L. Almar, H. Störmer, M. Meffert, J. Szász, F. Wankmüller, D. Gerthsen, E. I. Tiffée, *ACS Appl. Energy Mater.* **2018**, 1, 1316.

[103] D. S. Geng, N. Ding, T. S. A. Hor, S. W. Chien, Z. L. Liu, D. Wuu, X. L. Sun, Y. Zong, *Adv. Energy Mater.* **2016**, 6, 1502164.

[104] Y. Chen, S. Yoo, Y. M. Choi, J. H. Kim, Y. Ding, K. Pei, R. Murphy, Y. X. Zhang, B. T. Zhao, W. L. Zhang, H. J. Chen, Y. Chen, W. Yuan, C. H. Yang, M. L. Liu, *Energy Environ. Sci.* **2018**, 11, 2458.

[105] T. Fabiana, R. O'Hayre, S. Litster, F. B. Prinz, J. G. Santiago, *J. Power Sources* **2010**, 195, 3201.

[106] R. O'Hayre, T. Fabian, S. Litster, J. G. Santiago, F. B. Prinz, *J. Power Sources* 2007, 167, 118.

[107] T. Fabian, R. O'Hayre, F. B. Prinz, J. G. Santiago, *J. Electrochem. Soc.* **2007**, 154, B910.

[108] T. E. Springer, T. A. Zawodzinski, S. Gottesfeld, *J. Electrochem. Soc.* **1991**, 138, 2334.

[109] T. E. Springer, T. A. Zawodzinski, M. S. Wilson, S. Gottesfeld, *J. Electrochem. Soc.* **1996**, 143, 587.

[110] H Li, Y. H. Tang, Z. W. Wang, Z. Shi, S. H. Wu, D. T. Song, J. L. Zhang, K. Fatih, J. J. Zhang, H. J. Wang, Z. S. Liu, R. Abouatallah, A. Mazza, *J. Power Sources* **2008**, 178, 103.

[111] Q. Shen, J. Yang, K. L. Chen, H. Wang, J. B. Liu, H. Yan, *J. Solid State Electrochem.* **2016**, 20, 3331.

[112] T. V. Nguyen, D. Natarajan, R. Jain, *ECS Trans*. **2006**, 1, 501.

[113] D. P. Wilkinson, H. H. Voss, K. Prater, *J. Power Sources* **1994**, 49, 117.

[114] U. Pasaogullari, C. Y. Wang, *J. Electrochem. Soc.* **2005**, 152, A380.

[115] Q. Sun, J. Liu, X. Li, B. Q. Wang, H. Yadegari, A. Lushington, M. N. Banis, Y.

Zhao, W. Xiao, N. Chen, J. Wang, T. K. Sham, X. L. Sun, Adv. Funct. Mater. 2017, 27, 1606662.

[116] M. Shao, Q. Chang, J. P. Dodelet, R. Chenitz, Chem. Rev. 2016, 116, 3594.

[117] C. Chen, Y. Kang, Z. Huo, Z. Zhu, W. Huang, H. L. Xin, J. D. Snyder, D. Li, J. A. Herron, M. Mavrikakis, Science 2014, 343, 1339.

[118] S. Jiang, B. Yi, C. Zhang, S. Liu, H. Yu, Z. Shao, J. Power Sources 2015, 276, 80.

[119] W. Ding, Z. Wei, S. Chen, X. Qi, T. Yang, J. Hu, D. Wang, L.J. Wan, S. F. Alvi, L. Li, Angew. Chem. Int. Ed. 2013, 52, 11755.

[120] H. L. Lin, D. M. Chen, C. B. Lu, C. Zhang, F. Qiu, S. Han, X. D. Zhuang, Electrochim. Acta 2018, 266, 17.

[121] C. Tang, H. F. Wang, X. Chen, B. Q. Li, T. Z. Hou, B. Zhang, Q. Zhang, M. M. Titirici, F. Wei, Adv. Mater. 2016, 28, 6845.

[122] J. Zhang, Z. Zhao, Z. Xia, L. Dai, Nat. Nanotechn. 2015, 10, 444.

[123] T. Y. Ma, J. Ran, S. Dai, M. Jaroniec, S. Z. Qiao, Angew. Chem. Int. Ed. 2015, 54, 4646.

[124] H. Fei, R. Ye, G. Ye, Y. Gong, Z. Peng, X. Fan, E. L. G. Samuel, P. M. Ajayan, J. M. Tour, ACS Nano 2014, 8, 10837.

[125] C. You, X. Jiang, L. Han, X. Wang, Q. Lin, Y. Hua, C. Wang, X. Liu, S. Liao, J. Mater. Chem. A 2017, 5, 1742.

[126] L. Xu, H. Fan, L. X. Huang, J. L. Xia, S. H. Li, M. Li, H. Y. Ding, K. Huang, *Electrochim. Acta* **2017**, 239, 1.

[127] J. L. Ma, F. L. Meng, D. Xu, X. B. Zhang, *Energy Storage Mater.* **2017**, 6, 1.

[128] H. Luo, W. J. Jiang, Y. Zhang, S. Niu, T. Tang, L. B. Huang, Y. Y. Chen, Z. D. Wei, J. S. Hu, *Carbon* **2018**, 128, 97.

[129] N. Chandrasekaran, K. Selvakumar, V. PremKumar, S. Muthusamy, S. M. S. Kumar, R. Thangamuthu, *ACS Sustainable Chem. Eng.* **2018**, 6, 9094.

[130] M. Qiao, C. Tang, G. He, K. Qiu, R. Binions, I. P. Parkin, Q. Zhang, Z. Guo, M. M. Titirici, *J. Mater. Chem. A* **2016**, 4, 12658.

[131] G. L. Chai, K. P. Qiu, M. Qiao, *Energy Environ. Sci.* **2017**, 10, 1186.

[132] Q. D. Wang, Y. M. Li, K. Wang, J. T. Zhou, L. W. Zhu, L. Gu, J. Hu, X. B. Cao, *Electrochim. Acta* **2017**, 257, 250.

[133] Z. L. Zhang, C. Li, Y. Yamauchi, *Nano Today* **2016**, 11, 373.

[134] X. Liu, L. Dai, *Nat. Rev. Mater.* **2016**, 1, 16064.

[135] M. Z. Yu, S. Zhou, Y. Liu, Z. Y. Wang, T. Zhou, J. J. Zhao, Z. B. Zhao, J. S. Qiu, *Sci. China Mater.* **2017**, 60, 415.

[136] T. Reier, M. Oezaslan, P. Strasser, *ACS Catal.* **2012**, 2, 1765.

[137] M. Hunsom, D. Kaewsai, A. M. Kannan, *Intern. J. Hydrogen Energy* **2018**, 43, 21478.

[138] S. Luo, D. B. Zhou, *J. Electrochem. Soc.* **2013**, 161, A23.

[139] J. Ahmed, B. Kumar, A. M. Mugweru, P. Trinh, K. V. Ramanujachary, S. E. Lofland, A. K. Ganguli, *J. Phys. Chem. C* **2010**, 114, 18779.

[140] W. Bian, Z. Yang, P. Strasser, R. Yang, *J. Power Sources* **2014**, 250, 196.

[141] Y. C. Lu, H. A. Gasteiger, Y. S. Horn, *J. Am. Chem. Soc.* **2011**, 133, 19048.

[142] B. Sun, P. Munroe, G. Wang, *Sci. Rep.* **2013**, 3, 2247.

[143] B. G. Kim, H. J. Kim, S. Back, K. W. Nam, Y. Jung, Y. K. Han, J. W. Choi, *Sci. Rep.* **2014**, 4, 4225.

[144] S. M. Cho, S. W. Hwang, J. H. Yom, W. Y. Yoon, *J. Electrochem. Soc.* **2015**, 162, A2236.

[145] G. T. Fu, Z. M. Cui, Y. F. Chen, Y. T. Li, Y. W. Tang, J. B. Goodenough, *Adv. Energy Mater.* **2017**, 7, 1601172.

[146] Y. Yui, S. H. Sakamoto, M. Nohara, M. Hayashi, J. Nakamura, T. Komatsu, *J. Power Sources* **2017**, 340, 121.

[147] L. J. Wang, W. R. Dai, L. P. Ma, L. L. Gong, Z. Y. Lyu, Y. Zhou, J. Liu, M. Lin, M. Lai, Z. Q. Peng, W. Chen, *ACS Omega* **2017**, 2, 9280.

[148] F. Wu, Y. Xing, J. N. Lai, X. X. Zhang, Y. S. Ye, J. Qian, L. Li, R. J. Chen, *Adv. Funct. Mater.* **2017**, 27, 1700632.

[149] Z. L. Wang, D. Xu, J. J. Xu, X. B. Zhang, *Chem. Soc. Rev.* **2014**, 43, 7746.

[150] M. Xu, D. G. Ivey, Z. Xie, W. Qu, *J. Power Sources* **2015**, 283, 358.

[151] H. Zhao, C. Chen, D. J. Chen, M. Saccoccio, J. Wang, Y. Gao, T. H. Wan, F. Ciucci, *Carbon* **2015**, 90, 122.

[152] S. G. Mohamed, Y. Q. Tsai, C. J. Chen, Y. T. Tsai, T. F. Hung, W. S. Chang, R. S. Liu, *ACS Appl. Mater. Interfaces* **2015**, 7, 12038.

[153] N. N. Xu, J. L. Qiao, Q. Nie, M. Wang, H. Xu, Y. D. Wang, X. D. Zhou, *Catal. Today* **2018**, 318, 144.

[154] W. H. Ryu, T. H. Yoon, S. H. Song, S. Jeon, Y. J. Park, I. D. Kim, *Nano Lett.* **2013**, 13, 4190.

[155] W. W. Yin, Z. W. Fu, *Chem. Commun.* **2017**, 53, 1522.

[156] X. F. Hu, J. B. Wang, Z. F. Li, J. Q. Wang, D. H. Gregory, J. Chen, *Nano Lett.* **2017**, 17, 2073.

[157] R. H. Zhang, T. S. Zhao, P. Tan, M. C. Wu, H. R. Jiang, *Electrochim. Acta* **2017**, 257, 281.

[158] Y. Cheng, S. Dou, J. P. Veder, S. Y. Wang, M. Saunders, S. P. Jiang, *ACS Appl. Mater. Interfaces* **2017**, 9, 8121.

[159] J. B. Zhang, C. F. Zhang, W. Li, Q. Guo, H. C. Gao, Y. You, Y. T. Li, Z. M. Cui, K. C. Jiang, H. J. Long, D. W. Zhang, S. Xin, *ACS Appl. Mater. Interfaces* **2018**, 10, 5543.

[160] X. Xu, C. Su, W. Zhou, Y. Zhu, Y. Chen, Z. Shao, *Adv. Sci.* **2016**, 3, 1500187.

[161] M. H. Seo, H. W. Park, U. L. Dong, M. G. Park, Z. Chen, *ACS Catal.* **2015**, 5, 4437.

[162] F. Lu, J. Sui, J. Su, C. Jin, M. Shen, R. Yang, *J. Power Sources* **2014**, 271, 55.

[163] J. Sunarso, A. A. J. Torriero, W. Zhou, P. C. Howlett, M. Forsyth, *J. Phys. Chem. C* **2012**, 116, 5827.

[164] J. J. Xu, D. Xu, Z. L. Wang, H. G. Wang, L. L. Zhang, X. B. Zhang, *Angew. Chem. Int. Ed.* **2013**, 52, 3887.

[165] Y. J. Xue, H. Miao, S. S. Sun, Q. Wang, S. H. Li, Z. P. Liu, *J. Power Sources* **2017**, 342, 192.

[166] C. Gong, L. Zhao, S. Li, H. W. Wang, Y. S. Gong, R. Wang, B. B. He, *Electrochim. Acta* **2018**, 281, 338.

[167] Y. F. Bu, O. Gwon, G. Nam, H. Jang, S. Kim, Q. Zhong, J. Cho, G. Kim, *ACS Nano* **2017**, 11, 11594.

[168] Y. J. Zhao, Y. Hang, Y. D. Zhang, Z. D. Wang, Y. J. Yao, X. J. He, C. F. Zhang, D. W. Zhang, *Electrochim. Acta* **2017**, 232, 296.

[169] S. L. Li, Q. Xu, *Energy Environ. Sci.* **2013**, 6, 1656.

[170] W. Chaikittisilp, M. Hu, H. Wang, H. S. Huang, T. Fujita, K. C. W. Wu, L. C. Chen, Y. Yamauchi, K. Ariga, *Chem. Commun.* **2012**, 48, 7259.

[171] S. J. Yang, T. Kim, J. H. Im, Y. S. Kim, K. Lee, H. Jung, C. R. Park, *Chem. Mater.* **2012**, 24, 464.

[172] N. L. Torad, M. Hu, S. Ishihara, H. Sukegawa, A. A. Belik, M. Imura, K. Ariga, Y. Sakka, Y. Yamauchi, *Small* **2014**, 10, 2096.

[173] X. Zhang, S. W. Liu, Y. P. Zang, R. R. Liu, G. Q. Liu, G. Z. Wang, Y. X. Zhang, H. M. Zhang, H. J. Zhao, *Nano Energy* **2016**, 30, 93.

[174] J. S. Li, S. L. Li, Y. J. Tang, M. Han, Z. H. Dai, J. C. Bao, Y. Q. Lan, *Chem. Commun.* **2015**, 51, 2710.

[175] Q. L. Zhu, W. Xia, T. Akita, R. Zou, Q. Xu, *Adv. Mater.* **2016**, 28, 6391.

[176] S. Dou, X. Li, L. Tao, J. Huo, S. Wang, *Chem. Commun.* **2016**, 52, 9727.

[177] Y. H. Qian, Z. G. Hu, X. M. Ge, S. L. Yang, Y. W. Peng, Z. X. Kang, Z. L. Liu, J. Y. Lee, D. Zhao, *Carbon* **2017**, 111, 641.

[178] Z. T. Li, W. N. Zhao, C. Z. Yin, L. Q. Wei, W. T. Wu, Z. P. Hu, M. B. Wu, *ACS Appl. Mater. Interfaces* **2017**, 9, 44519.

[179] Y. S. Liu, H. Jiang, J. Y. Hao, Y. L. Liu, H. B. Shen, W. Z. Li, J. Li, *ACS Appl.*

Mater. Interfaces **2017**, 9, 31841.

[180] D. S. Raja, X. F. Chuah, S. Y. Lu, *Adv. Energy Mater.* **2018**, 8, 1801065.

[181] Z. B. Liang, C. Qu, D. G. Xia, R. Q. Zou, Q. Xu, *Angew. Chem.* **2018**, 130, 9750.

[182] H. Fei, J. Dong, M. J. Arellano-Jimenez, G. Ye, N. D. Kim, E. L. G. Samuel, Z. Peng, Z. Zhu, F. Qin, J. Bao, M. J. Yacaman, P. M. Ajayan, D. Chen, J. M. Tour, *Nat. Commun.* **2015**, 6, 8668.

[183] C. Lecuyer, F. Quignard, A. Choplin, D. Olivier, J. M. Basset, *Angew. Chem., Int. Ed.* **1991**, 30, 1660.

[184] H. X. Zhong, J. Wang, Y. W. Zhang, W. L. Xu, W. Xing, D. Xu, Y. F. Zhang, X. B. Zhang, *Angew. Chem.* **2014**, 126, 14459.

[185] R. Lang, T. Li, D. Matsumura, S. Miao, Y. Ren, Y. Cui, Y. Tan, B. Qiao, L. Li, A. Wang, X. Wang, T. Zhang, *Angew. Chem. Int. Ed.* **2016**, 55, 16054.

[186] Y. Peng, B. Z. Lu, S. W. Chen, *Adv. Mater.* **2018**, 30, 1801995.

[187] P. Z. Chen, T. P. Zhou, L. L. Xing, K. Xu, Y. Tong, H. Xie, L. D. Zhang, W. S. Yan, W. S. Chu, C. Z. Wu, Y. Xie, *Angew. Chem. Int. Ed.* **2016**, 55, 1.

[188] Y. H. Han, Y. G. Wang, W. X. Chen, R. R. Xu, L. R. Zheng, J. Zhang, J. Luo, R. A. Shen, Y. Q. Zhu, W. C. Cheong, C. Chen, Q. Peng, D. S. Wang, Y. D. Li, *J. Am. Chem. Soc.* **2017**, 139, 17269.

[189] W. Wei, X. M. Shi, P. Gao, S. S. Wang, W. Hu, X. X. Zhao, Y. M. Ni, X. Y. Xu, Y. Q. Xu, W. S. Yan, H. X. Ji, M. H. Cao, *Nano Energy* **2018**, 52, 29.

[190] H. X. Xu, D. J. Cheng, D. P. Cao, X. C. Zeng, *Nat. Catal.* **2018**, 1, 339.

[191] C. Z. Zhu, S. F. Fu, J. H. Song, Q. R. Shi, D. Su, M. H. Engelhard, X. L. Li, D.

D. Xiao, D. S. Li, L. Estevez, D. Du, Y. L. Lin, *Small* **2017**, 13, 1603407.

[192] H. J. Shen, E. Gracia-Espino, J. Y. Ma, K. T. Zang, J. Luo, L. Wang, S. S. Gao, X. Mamat, G. Z. Hu, *Angew.Chem. Int. Ed.* **2017**, 56, 13800.

[193] P. Q. Yin, T. Yao, Y. Wu, L. R. Zheng, Y. Lin, W. Liu, H. X. Ju, J. F. Zhu, X. Hong, Z. X. Deng, G. Zhou, S. Q. Wei, Y. D. Li, *Angew. Chem. Int. Ed.* 2016, 55, 10800.

[194] H. G. Zhang, S. Hwang, M. Y. Wang, Z. X. Feng, S. Karakalos, L. L. Luo, Z. Qiao, X. H. Xie, C. M. Wang, D. Su, Y. Y. Shao, G. Wu, *J. Am. Chem. Soc.* **2017**, 139, 14143.

[195] X. F. Yang, A. Q. Wang, B. T. Qiao, J. Li, J. Y. Liu, T. Zhang, *Acc. Chem. Res.* **2013**, 46, 1740.

[196] B. T. Qiao, A. Q. Wang, X. F. Yang, L. F. Allard, Z. Jiang, Y. T. Cui, J. Y. Liu, J. Li, T. Zhang, *Nat. Chem.* **2011**, 3, 634.

[197] R. Lv, J. A. Robinson, R. E. Schaak, D. Sun, Y. Sun, T. E. Mallouk, M. Terrones, *Acc. Chem. Res.* **2015**, 48, 56.

[198] S. Liu, Y. Ying, M. Wu, K. S. Hui, K. N. Hui, C. Y. Ouyang, S. C. Jun, *Small* **2019**, 15, 1803984.

[199] S. P. Zhang, Z. N. Huang, Z. Y. Wen, L. L. Zhang, J. Jin, R. S. Yassar, J. H. Yang, Nano Lett. 2017, 17, 3518.

[200] Z. M. Cui, Y. T. Li, G. T. Fu, X. Li, J. B. Goodenough, *Adv. Mater.* **2017**, 29, 1702385.

[201] B. Huang, Y. Liu, Z. Xie, *J. Mater. Chem. A* **2017**, 5, 23481.

[202] L. Y. Jiang, X. X. Lin, A. J. Wang, J. H. Yuan, J. J. Feng, X. S. Li, *Electrochim.*

Acta **2017**, 225, 525.

[203] Y. J. Xue, S. S. Sun, Q. Wang, H. Miao, S. H. Li, Z. P. Liu, *Electrochim. Acta* **2017**, 230, 418.

[204] J. Fu, Z. P. Cano, M. G. Park, A. P. Yu, M. Fowler, Z. W. Chen, *Adv. Mater.* **2017**, 29, 1604685.

[205] Q. W. Tang, L. M. Wang, M. J. Wu, N. N. Xu, L. Jiang, J. L. Qiao, *J. Power Sources* **2017**, 365, 348.

[206] S. M. Chen, J. Y. Cheng, L. T. Ma, S. K. Zhou, X. W. Xu, C. Y. Zhi, W. J. Zhang, L. J. Zhi, J. A. Zapien, *Nanoscale* **2018**, 10, 10412.

[207] H. Li, Q. Li, P. Wen, T. B. Williams, S. Adhikari, C. C. Dun, C. Lu, D. Itanze, L. Jiang, D. L. Carroll, G. L. Donati, P. M. Lundin, Y. Y. Qiu, S. M. Geyer, *Adv. Mater.* **2018**, 30, 1705796.

[208] J. Hu, Q. N. Liu, L. N. Shi, Z. W. Shi, H. Huang, *Appl. Surf. Sci.* **2017**, 402, 61.

[209] J. Park, M. Risch, G. Nam, M. Park, T. J. Shin, S. Park, M. G. Kim, Y. S. Horn, J. Cho, *Energy Environ. Sci.* **2017**, 10, 129.

[210] Z. Y. Chen, Y. N. Li, L. L. Lei, S. J. Bao, M. Q. Wang, H. Liu, Z. L. Zhao, M. W Xu, *Catal. Sci. Technol.* **2017**, 7, 5670.

[211] Y. T. Tan, L. Meng, Y. Q. Wang, W. J. Dong, L. B. Kong, L. Kang, F. Ran, *Electrochim. Acta* **2018**, 277, 41.

[212] W. Li, C. Y. Cao, C. Q. Chen, Y. Zhao, W. G. Song, L. Jiang, *Chem. Commun.* **2011**, 47, 3619.

[213] F. A. A. Ruiter, C. Alexander, F. R. A. J. Rose, J. I. Segal, *Biomed. Mater.* **2017**,

12, 055009.

[214] J. A. Park, S. B. Kim, *Chemosphere* **2017**, 167, 469.

[215] M. Raufa, J. W. Wang, P. X. Zhang, W. Iqbal, J. Qu, Y. L. Li, *J. Power Sources* **2018**, 408, 17.

[216] N. Tam, S. Oguz, A. Aydogdu, G. Sumnu, S. Sahin, *Food Res. Int.* **2017**, 102, 616.

[217] C. Ribeiro, V. Sencadas, J. L. G. Ribelles, S. L. Méndez, *Soft Mater.* **2010**, 8, 274.

[218] Q. Y. Wang, Q. F. Lu, M. Z. Wei, E. Y. Guo, L. B. Yao, K. Sun, *J. Sol-Gel Sci. Techn.* **2018**, 85, 84.

[219] Z. D. Liu, Q. F. Lu, M. Z. Wei, E. Y. Guo, *J. Sol-Gel Sci. Techn.* **2017**, 82, 67.

[220] Q. Y. Wang, K. Sun, Q. F. Lu, M. Z. Wei, L. B. Yao, E. Y. Guo, *Dyes and Pigments* **2018**, 155, 194.

[221] Q. Y. Wang, Q. F. Lu, X. Y. Ji, Z. D. Liu, M. Z. Wei, E. Y. Guo, *J. Nanopart. Res.* **2017**, 19, 222.

[222] Y. Cao, H. M. Lu, Q. S. Hong, J. J. Bai, J. R. Wang, X. D. Li, *J. Power Sources* **2017**, 368, 78.

[223] Y. Wang, J. Fu, Y. N. Zhang, M. Li, F. M. Hassan, G. Li, Z. W. Chen, *Nanoscale* **2017**, 9, 15865.

[224] X. L. Zhang, Y. D. Gong, S. Q. Li, C. W. Sun, *ACS Catal.* **2017**, 7, 7737.

[225] X. J. Wang, Y. Li, T. Jin, J. Meng, L. F. Jiao, M. Zhu, J. Chen, *Nano Lett.* **2017**, 17, 7989.

[226] Y. X. Zhao, Q. X. Lai, J. J. Zhu, J. Zhong, Z. M. Tang, Y. Luo, Y. Y. Liang, *Small* **2018**, 14, 1704207.

[227] C. Alegre, C. Busacca, O. D. Blasi, V. Antonucci, A. S. Aricò, A. D. Blasi, V. Baglio, *J. Power Sources* **2017**, 364, 101.

[228] R. L. Puurunen, *J. Appl. Phys.* **2005**, 97, 121301.

[229] H. J. Shin, D. K. Jeong, J. G. Lee, M. M. Sung, J. Y. Kim, *Adv. Mater.* **2004**, 16, 1197.

[230] C. Guan, J. Wang, *Adv. Sci.* **2016**, 3, 1500405.

[231] X. Xia, Y. Wang, D. Wang, Y. Zhang, Z. Fan, J. Tu, H. Zhang, H. J. Fan, *Nano Energy* **2016**, 20, 244.

[232] C. Guan, J. Liu, Y. Wang, L. Mao, Z. Fan, Z. Shen, H. Zhang, J. Wang, *ACS Nano* **2015**, 9, 5198.

[233] Y. Lei, J. Lu, X. Y. Luo, T. P. Wu, P. Du, X. Y. Zhang, Y. Ren, J. G. Wen, D. J. Miller, J. T. Miller, Y. K. Sun, J. W. Elam, K. Amine, *Nano Lett.* **2013**, 13, 4182.

[234] J. Xie, X. Yao, I. P. Madden, D. E. Jiang, L. Y. Chou, C. K. Tsung, D. Wang, *J. Am. Chem. Soc.* **2014**, 136, 8903.

[235] M. A. Schroeder, A. J. Pearse, A. C. Kozen, X. Chen, K. Gregorczyk, X. Han, A. Cao, L. Hu, S. B. Lee, G. W. Rubloff, M. Noked, *Chem. Mater.* **2015**, 27, 5305.

[236] N. Cheng, M. N. Banis, J. Liu, A. Riese, X. Li, R. Li, S. Ye, S. Knights, X. Sun, *Adv. Mater.* **2015**, 27, 277.

[237] N. Cheng, M. N. Banis, J. Liu, A. Riese, S. Mu, R. Li, T. K. Sham, X. Sun, *Energy Environ. Sci.* **2015**, 8, 1450.

[238] J. Lu, Y. Lei, K. C. Lau, X. Y. Luo, P. Du, J. G. Wen, R. S. Assary, U. Das, D. J. Miller, J. W. Elam, H. M. Albishri, D. A. E. Hady, Y. K. Sun, L. A. Curtiss, K. Amine,

Nat. Commun. **2013**, 4, 2383.

[239] H. Li, Z. Guo, X. W. Wang, *J. Mater. Chem. A* **2017**, 5, 21353.

[240] X. L. Xu, H. Wang, Y. Z. Xie, J. B. Liu, H. Yan, W. Liu, *J. Electrochem. Soc.* **2018**, 165, A2978.

[241] C. C. Zhao, X. X. Yan, G. Q. Wang, Y. H. Jin, X. Du, W. B. Du, L. Sun, C. W. Ji, *Intern. J. Hydrogen Energy* **2018**, 43, 5001.

[242] Z. Khan, S. O. Park, J. C. Yang, S. Park, R. Shanker, H. K. Song, Y. Kim, S. K. Kwak, H. Ko, *J. Mater. Chem. A* **2018**, 6, 24459.

[243] L. Song, T. Wang, L. H. Li, C. Wu, J. P. He, *Appl. Catal. B-Environ.* **2019**, 244, 197.

[244] S. S. Shinde, C. H. Lee, J. Y. Jung, N. K. Wagh, S. H. Kim, D. H. Kim, C. Lin, S. U. Lee, J. H. Lee, *Energy Environ. Sci.* **2019**, 12, 727.